Design and Performance of Huffman Sequences in Medical Ultrasound Coded Excitation

Alessandro Polpetta, *Student Member, IEEE*, and Paolo Banelli, *Member, IEEE*

***Abstract*—This paper deals with coded-excitation techniques for ultrasound medical echography. Specifically, linear Huffman coding is proposed as an alternative approach to other widely established techniques, such as complementary Golay coding and linear frequency modulation. The code design is guided by an optimization procedure that boosts the signal-to-noise ratio gain (GSNR) and, interestingly, also makes the code robust in pulsed-Doppler applications. The paper capitalizes on a thorough analytical model that can be used to design any linear coded-excitation system. This model highlights that the performance in frequency-dependent attenuating media mostly depends on the pulse-shaping waveform when the codes are characterized by almost ideal (i.e., Kronecker delta) autocorrelation. In this framework, different pulse shapers and different code lengths are considered to identify coded signals that optimize the contrast resolution at the output of the receiver pulse compression. Computer simulations confirm that the proposed Huffman codes are particularly effective, and that there are scenarios in which they may be preferable to the other established approaches, both in attenuating and non-attenuating media. Specifically, for a single scatterer at 150 mm in a 0.7-dB/(MHz·cm) attenuating medium, the proposed Huffman design achieves a main-to-side lobe ratio (MSR) equal to 65 dB, whereas tapered linear frequency modulation and classical complementary Golay codes achieve 35 and 45 dB, respectively.**

I. Introduction

Ultrasound echography is a medical imaging technique that is often used for diagnostic purposes, mostly because of its safety and simplicity of use. The quality of ultrasound images is assessed by performance measures such as the spatial resolution, penetration depth, SNR, and contrast resolution. Typically, these performance measures depend on trade-offs between ultrasound physical parameters (e.g., frequency, bandwidth, transmitted power) and the specific beamforming technique that is used [1]. For instance, for a given transmitted power, high-frequency ultrasound is characterized by better lateral resolution, which is proportional to the signal wavelength [1], [2]. Note that the lateral resolution contributes to the overall spatial resolution together with the axial resolution, which depends on the signal bandwidth. However, as will be clarified in Section II, frequency-dependent attenuation in high-frequency ultrasound induces a shorter penetration depth and a lower SNR. In practice, it is difficult to compensate for this decrease in penetration depth by increasing the amplitude of the transmitted ultrasound, which is limited by the cost of pulse generator and transducer, as well as by patient safety, because of the increase of the tissue temperature [3]–[7]. Consequently, it is difficult to obtain high penetration depth with high spatial resolution.

A possible approach to improve the penetration depth and SNR is the use of coded-excitation (CE) methods [8]–[16], i.e., to excite the ultrasound transducer with a long modulated pulse. This long excitation increases the transmitted energy without increasing the pulse amplitude; however, a long excitation would also degrade the axial resolution, which is restored by pulse compression at the receiving end. In practice, the pulse duration can be extended up to certain limits, which are imposed by regulatory agencies for patient safety, as clarified in [17], [18], and references therein. Actually, the CE approach, which has been widely used in electromagnetic radar system design [19], has not been fully exploited for ultrasound medical applications because of the problems arising from non-isolated target detection, speckle, frequency-dependent attenuation of the human body, lower system bandwidth imposed by piezoelectric transducers, and limited durations of transmission [8].

Only in the recent past, researchers renewed their interest for CE schemes for medical ultrasounds, and different techniques have been proposed [8]–[16], [20]–[23]. Most of them focused on linear frequency-modulation (FM) (i.e., chirp) codes coupled with pre-enhancement and bandwidth enlargement techniques [8]–[11], [20]–[23]. Alternatively, other authors proposed single- [12] and double-transmission [13], [14] phase-modulating codes, which are attractive for their low hardware implementation complexity. Conversely, in the previous decade, researchers refrained from using amplitude-modulating codes in ultrasound because of the technical challenges associated with the physical generation of ultrasound signals with variable amplitude [24] and, still recently, because of the lower average energy that is possible to transmit. However, the sharp (i.e., 12-bit) amplitude resolution that is possible in recent ultrasound systems, such as those exploiting linear-FM transmissions (e.g., nonlinear codes with constant amplitude) [15], and the availability of optimization procedures to boost the transmitted signal energy [25], are good arguments to further explore the use of linear codes with non-constant amplitudes for ultrasound im-

Manuscript received July 14, 2011; accepted January 10, 2012.

The authors are with the Department of Electronic and Information Engineering, University of Perugia, Perugia, Italy (e-mail: paolo.banelli@diei.unipg.it).

DOI: http://dx.doi.org/10.1109/TUFFC.2012.2242

aging. Actually, constant-amplitude complementary Golay codes [13], [14], which cancel side lobes by using two complementary excitations, provide optimal performance in frequency-flat environments (commonly referred to as non-attenuating media). However, Golay codes suffer from a performance degradation in the presence of frequency-dependent attenuation [16] and they are not robust to the frequency-shifts induced in pulsed-Doppler applications. On the contrary, linear-FM codes [16], which are robust to frequency-dependent attenuation, suffer from a non-ideal (e.g., non-Kronecker-Delta) autocorrelation function in frequency-flat environments and, consequently, are characterized by a certain degradation in contrast resolution. Motivated by the goal of a CE technique that could guarantee the quasi-absence of side lobes, both in the presence and in the absence of frequency-dependent attenuation, the authors recently proposed in [26] to generate the ultrasound signal by using Huffman codes, which are complex sequences that combine amplitude with phase (and thus frequency) coding. This paper extends the preliminary results obtained in [26], by

1) developing an accurate analytical model to guide the parameter optimization;
2) comparing the proposed scheme (and establishing connection) with state-of-the-art linear-FM codes and double-transmission complementary Golay codes;
3) simulating B-mode images that highlight the merits of the proposed approach in critical scenarios.

Capitalizing on the rigorous analytical model, this paper discusses the design of any linear CE system, and clarifies some misleading beliefs with respect to design criteria in frequency-dependent attenuating media. Specifically, Section II provides details of a typical CE architecture and describes the signal model, whereas Section III focuses on the analytical design of various coded waveforms. Section IV illustrates the Huffman coding theory and its optimization [27]. Then, Section V tests the proposed Huffman coding approach by means of typical ultrasound performance indices and compares the results with those of linear-FM [16] and complementary Golay coded systems [14]. To further corroborate the theoretical design, the overall performance of the proposed excitation scheme is evaluated for B-mode images in Section VI through the use of the Field II model [28]. Finally, conclusions and open research problems are summarized in Section VII.

II. System Architecture and Signal Model

Fig. 1 describes the block diagram of a CE ultrasound system that employs a phased-array probe with Q piezoelectric elements.

CE is a transmission technique that exploits ultrasound pulses with a time-bandwidth product (TBP) greater than one. In medical ultrasound, the increase of TBP is obtained by an increase of the pulse duration, because the bandwidth of the voltage signal that drives the ultrasound transducer should match the limited ultrasound frequencies the transducer can generate. Referring to Fig. 1, at every pulse repetition period, the code generator produces the discrete-time baseband signal

$$\tilde{s}[n] = a[n]e^{j\phi[n]}, \tag{1}$$

where $a[n]$ and $\phi[n]$ are the signal amplitude and the phase, respectively. Thus, if T_s is the sampling interval, the discrete-time RF signal $s[n] = s(nT_\mathrm{s})$ is simply expressed by

$$s[n] = \Re\{\tilde{s}[n]e^{j2\pi f_0 T_s n}\}, \quad n \in [0, \Delta_\mathrm{s}], \tag{2}$$

where f_0 is the ultrasound center frequency, $f_\mathrm{s} = 1/T_\mathrm{s}$ is the signal generation frequency, Δ_s is the discrete-time duration of the CE pulse, and $\Re\{x\}$ is the real part of a complex number x. The analog signal $s(t)$, obtained from $s[n]$ by digital-to-analog conversion (DAC), is successively amplified through a high-voltage (HV) driver, whose aim is to adjust the signal dynamic range to that of the transducer.

At the receiver side, the ultrasound is converted into electric voltage by the piezoelectric element, whose output is processed and amplified by dedicated analog circuitry. In the presence of a single scatterer, whose round-trip distance from the transducer is $\vec{r}$, the received signal $r(t)$ is the time-shifted version of the convolution between the transmitted signal $s(t)$ and the system impulse response $h_\mathrm{tot}(t, \vec{r})$, as expressed by

$$r(t) = s(t - \tau_0) * h_\mathrm{tot}(t, \vec{r}) + \mu(t), \tag{3}$$

where $\tau_0 = |\vec{r}|/c$ is the round-trip delay when c is the ultrasound velocity in the tissue, $*$ is the convolution operator, and $\mu(t)$ represents the system noise. In [29], it is shown that the system impulse response $h_\mathrm{tot}(t, \vec{r})$ depends on the temporal and spatial impulse responses of the transducer, $h_\mathrm{t}(t)$ and $h_\mathrm{s}(t, \vec{r})$, respectively, and on the tissue frequency-dependent attenuation $h_\mathrm{att}(t, \vec{r})$, as expressed by

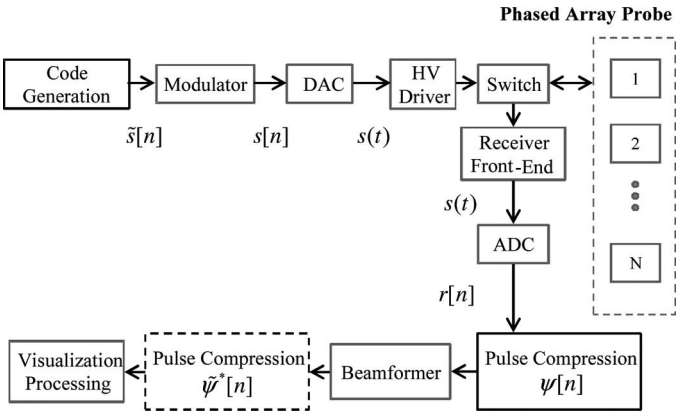

Fig. 1. Block diagram of a coded-excitation ultrasound phased-array system.

$$h_{\mathrm{tot}}(t,\vec{r}) = h_{\mathrm{t}}(t) * h_{\mathrm{s}}(t,\vec{r}) * h_{\mathrm{att}}(t,\vec{r}). \tag{4}$$

In (4), $h_{\mathrm{att}}(t,\vec{r})$ is the inverse Fourier transform of $H_{\mathrm{att}}(f,\vec{r})$, whose dependence on the frequency f is typically expressed by [29], [30]

$$H_{\mathrm{att}}(f,\vec{r}) = e^{-\alpha|\vec{r}|}e^{-\beta(f-f_0)|\vec{r}|}e^{-j2\pi f(\tau_{\mathrm{b}}+\tau_{\mathrm{m}}(\beta/\pi^2)|\vec{r}|)}e^{j2(f/\pi)\beta|\vec{r}|ln(2\pi f)}, \tag{5}$$

where $\tau_{\mathrm{b}} = 1/c$ is the bulk propagation delay per unit length, τ_{m} is the minimum phase delay factor, and α and β are the coefficients associated with the frequency-independent and frequency-dependent attenuation, respectively. Specifically, $\tau_{\mathrm{m}} = 20$ has been used to fit the dispersion found in the tissue, as suggested by [30]. Instead of using (3), in [8], [16], and [31]–[33], it is suggested that the effect of a frequency-dependent attenuation can be approximated by a frequency down-shift of the transmitted signal, as expressed by

$$r_{\mathrm{app}}(t) \approx e^{-\alpha|\vec{r}|}s(t-\tau_0)e^{j2\pi[-f_{\mathrm{d}}(t-\tau_0)]} + \mu(t), \tag{6}$$

where, for a transmitted pulse with relative bandwidth B_{r}, the frequency shift f_{d} induced by the frequency-dependent attenuation [8] is usually approximated by [32]

$$f_{\mathrm{d}} = \beta B_{\mathrm{r}}^2 f_0^2 |\vec{r}|. \tag{7}$$

Actually, this approximation, which neglects the compression of the spectrum bandwidth, may be acceptable when the pulse waveform is almost Gaussian, and when the frequency-dependent attenuation is characterized by a quadratic law [34], [32]. This paper will clarify that this is not the case in general and that caution should be used in employing (6) for design purposes.

The discrete-time RF received signal $r[n] = r(nT_{\mathrm{s}})$ is obtained by analog-to-digital conversion (ADC), where, for simplicity of notation, it is assumed that the sampling interval T_{s} is the same one used in the generation process. Note that, the pulse compression block may be inserted either after, or before, the beamforming block in the receive chain, as shown in Figs. 2 and 3, respectively. It is evident that the solution in Fig. 2 has a lower computational complexity than the solution in Fig. 3.

However, the low-complexity configuration of Fig. 2, which employs a single decoding block instead of Q parallel pulse compressors, involves some distorting effects resulting from the dynamic focusing beamforming. These effects are investigated in [35] and detailed in [36], where possible solutions to limit such distortions are also suggested. To avoid constraints on the code lengths and on the TBP that would be more stringent than those already imposed by the dead-zone width (see [35] for further details), and to better highlight the role played by Huffman coding, this paper considers the more complex receive architecture shown in Fig. 3, leaving the study of the interplay with dynamic focusing effects for future investigations.

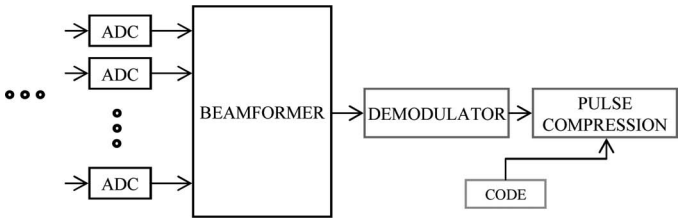

Fig. 2. Low-complexity receive block diagram.

Using the approach described in Fig. 3, the discrete-time RF signal $r[n]$ may be processed to compress (decode) the effective impulse response, and consequently restore the spatial resolution. If not otherwise specified, $R_{xy}[n]$ indicates the classical cross-correlation function of two generic digital waveforms $x[n]$ and $y[n]$. Thus, the output of the pulse compression block in Fig. 1 is obtained by cross-correlating the received waveform $r[n]$ with a pulse compression waveform $\psi[n]$, as expressed by

$$\begin{aligned} R_{r\psi}[n] &= \sum_{m=-\infty}^{+\infty} r[m]\psi[n+m] \\ &= \left|\tilde{R}_{r\psi}[n]\right|\cos(2\pi f_0 n T_s + \angle(\tilde{R}_{r\psi}[n])). \end{aligned} \tag{8}$$

Eq. (8) can be summarized by its baseband counterpart

$$\tilde{R}_{r\psi}[n] = \sum_{m=-\infty}^{+\infty} \tilde{r}^*[m]\tilde{\psi}[n+m], \tag{9}$$

where $\tilde{r}[n]$ and $\tilde{\psi}[n]$ are the complex envelope associated with the received signal $r[n] = \Re\{\tilde{r}[n]e^{j2\pi f_0 T_s n}\}$ and the RF compression waveform $\psi[n] = \Re\{\tilde{\psi}[n]e^{j2\pi f_0 T_s n}\}$, respectively. Eq. (9) depends on the transmitted signal $s(t)$ by (3) and, in the absence of frequency-dependent attenuation (i.e., $\beta = 0$), the discrete-time received signal can be expressed by

$$r[n] = e^{-\alpha|\vec{r}|}s[n-n_0] + \mu[n], \tag{10}$$

i.e., an attenuated and delayed version of the transmitted signal $s[n]$ with discrete-time delay $n_0 = \lceil \tau_0 f_s \rfloor$, where $\lceil x \rfloor$ represents the approximation of a number x to its nearest integer. Thus, the RF pulse compression output would be simply $R_{r\psi}[n] = e^{-\alpha|\vec{r}|}R_{s\psi}[n+n_0] + R_{\mu\psi}[n]$.

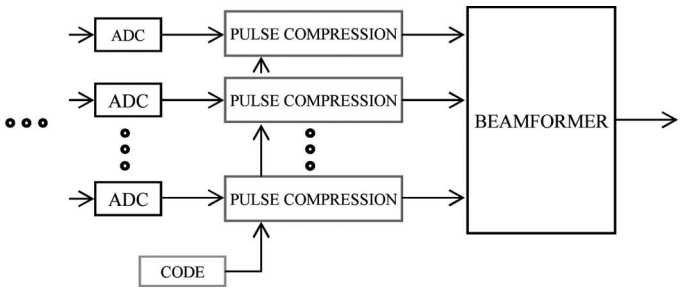

Fig. 3. High-complexity receive block diagram.

However, when $\beta \neq 0$, by means of the approximation in (6), the discrete-time received signal would become

$$r_{\text{app}}[n] = e^{-\alpha|\vec{r}|}s[n-n_0]e^{-j2\pi f_{\text{d}}(n-n_0)T_{\text{s}}} + \mu[n], \quad (11)$$

which would give a pulse compression output $R_{r\psi,\text{app}}[n]$, expressed by

$$\begin{aligned} R_{r\psi,\text{app}}[n] &\approx \sum_{m=-\infty}^{+\infty} e^{-\alpha|\vec{r}|}s[m-n_0]\psi[n+m]e^{-j2\pi f_{\text{d}}(m-n_0)T_{\text{s}}} \\ &\quad + R_{\mu\psi}[n] \\ &\approx e^{-\alpha|\vec{r}|}\chi_{s\psi}(n+n_0, f_{\text{d}}) + R_{\mu\psi}[n]. \end{aligned} \quad (12)$$

In this view, and by means of the approximation in (6), to evaluate the coding performance in practical scenarios, some authors propose in [8], [16], [32], and [33] to not consider the simple baseband correlation function $\tilde{R}_{s\psi}[n]$, but more generally, the baseband ambiguity function

$$\tilde{\chi}_{s\psi}(n, f_{\text{d}}) = \sum_{m=-\infty}^{+\infty} \tilde{s}^*[m]\tilde{\psi}[m+n]e^{-j2\pi f_{\text{d}}mT_{\text{s}}}. \quad (13)$$

Indeed, $\tilde{\chi}_{s\psi}(n, f_{\text{d}})$ is a 2-D function that shows how the perceived cross-correlation function changes with a frequency shift f_{d}, and it subsumes the correlation function by $\tilde{R}_{s\psi}[n] = \tilde{\chi}_{s\psi}(n, 0)$.

Actually, the ambiguity function $\tilde{\chi}_{s\psi}(n, f_{\text{d}})$ can approximate the pulse compression output in the presence of frequency-dependent attenuating media, only if the assumptions of Gaussian pulse-shaper, and quadratic frequency-dependent attenuation, hold true [34]. Indeed, the frequency-dependent attenuation introduces a higher attenuation of the higher frequencies, which may be interpreted as a virtual down-shift f_{d} of the centrum frequency. Actually, although this virtual down-shift affects the spectrum magnitude, it is not generally the case for the spectrum phase of the transmitted signal and, consequently, such an approximation is still acceptable only when the spectrum phase is linear. Thus, the other constraint for the approximation to hold true is that the spectrum phase should be linear. For this reason, both in the case of frequency and phase CE, the ambiguity function should not be used to design the code or to assess performance. This fact is also confirmed by the simulation results in Section IV, which show that excitation codes characterized by very different ambiguity functions conversely provide almost the same pulse compression performance in frequency-dependent attenuating media.

Thus, by means of (3), the discrete-time received signal $r[n]$ is modeled by

$$r[n] = s[n-n_0] * h_{\text{tot}}(n, \vec{r}) + \mu[n], \quad (14)$$

where $h_{\text{tot}}(n, \vec{r})$ is the discrete-time counterpart of (4). The ambiguity function is fundamental to assess the ultrasound imaging performance in pulsed-Doppler applications. Indeed, the velocity v_{b} of blood reflecting particles induces a Doppler shift f_{d}, which depends on the ultrasound velocity v_{u}, and on the angle θ between the direction of the flow and the ultrasound beam, by [32]

$$f_{\text{d}} = 2f_0 \frac{v_{\text{b}}}{v_{\text{u}}} \cos(\theta). \quad (15)$$

In the absence of frequency-dependent attenuation, the presence of such a Doppler shift f_{d} causes the pulse compression output $R_{r\psi}[n]$ to be equal to the ambiguity function $\chi_{s\psi}(n, f_{\text{d}})$.

III. Ultrasound Coded-Excitation

The design of a CE system consists of the design of a coding vector $\mathbf{c} = [c_0, c_1, \ldots, c_N]$ such that the baseband signal $\tilde{s}[n]$ associated with $s(t)$ can be represented by a function of the coding sequence $\mathbf{c}$, as expressed by

$$\tilde{s}[n] = f_{\text{s}}(\mathbf{c}). \quad (16)$$

The proper selection of the code $\mathbf{c}$ and of the function $f_{\text{s}}(\cdot)$ has to be guided by a careful analysis of performance and hardware requirements in the perspective of clinical applications. For instance, in ultrasound B-mode imaging, the code performance is typically summarized by the complex pulse compression output $\tilde{R}_{r\psi}[n]$. More precisely, typical parameters are the axial resolution, which can be measured as the -20-dB width of the main lobe of $|\tilde{R}_{r\psi}[n]|$ [37], and the contrast resolution, which depends on the main-to-side lobe ratio (MSR) of $|\tilde{R}_{r\psi}[n]|$, as well as on the SNR and the dynamic range [37]. When the compression waveform $\psi[n]$ is equal to the transmitted signal $s[n]$, the pulse compression is the classical matched-filter and thus it would be $\tilde{R}_{r\psi}[n] = \tilde{R}_{rs}[n]$. Very frequently, the compression waveform $\psi[n]$ is obtained by either a time or a frequency windowing of the transmitted signal $s[n]$, realizing a mismatched filtering, which is widely used in [16] and accurately explained in [38]. Although the SNR is amplified by a factor up to the TBP in CE, after decoding, the acoustic energy could remain partially distributed in time (and thus in space): this is indicated by an enlargement of the main lobe and by the generation of range lobes that reduce both the axial and the contrast resolution.

Together with the axial and the contrast resolutions, another important parameter to measure the quality of the performance is the SNR gain (GSNR), defined by [19]

$$\text{GSNR} = \frac{\text{SNR}_{\text{c}}}{\text{SNR}_0} = \frac{\max\limits_n(|R_{r\psi}[n]|)}{\max\limits_n(|R_{\psi\psi}[n]|)\sigma^2} \frac{\max\limits_n(|R_{s_0s_0}[n]|)\sigma^2}{\max\limits_n(|R_{r_0s_0}[n]|)}, \quad (17)$$

where $\max\limits_n(x[n])$ represents the largest element in $x[n]$. In (17), σ^2 is the system noise power, SNR_{c} is the SNR guar-

anteed by the CE technique in (16) with a pulse compression waveform $\psi[n]$, whereas SNR_0 is the SNR of the received signal $r_0[n]$ that corresponds to the transmission (without CE) of a single pulse $s_0[n] = \sin[2\pi f_0 n]$, with $n \in [0, \lfloor f_s/B \rfloor]$, and where B is the pulse bandwidth. Moreover, to avoid performance degradation in the case of moving blood reflecting particles, it is necessary to design a code with a ridge-like ambiguity function. This is what happens, for instance, by using a linear-FM modulation (chirp), expressed by

$$s^{(c)}[n + \Delta_s/2] = \cos\left(2\pi \frac{f_0}{f_s} n + \frac{\pi B}{\Delta_s f_s} n^2\right), \quad n \in [0, \Delta_s], \tag{18}$$

which [see (16)], represents a non-linear coding at RF.

A. Linear Coded-Excitation

Indicating with $\{c_i\}_{i=0,\ldots,N}$ the entries (commonly called chips) of the code vector $\mathbf{c}$ and with $\delta[n]$ the Kronecker delta function, let us define $\hat{c}[n]$, the normalized and upsampled (zero-filled) version of the code $\mathbf{c}$ with upsampling factor M, as expressed by

$$\hat{c}[n] = \frac{1}{c_{\max}} \sum_{i=0}^{N} c_i \delta[n - iM], \tag{19}$$

where $c_{\max} = \max_n\{|c_i|\}$. Then, a linear coded excitation (LCE) is expressed by the convolution of $\hat{c}[n]$ with the pulse shaping waveform $p[n]$,

$$\tilde{s}^{(L)}[n] = f_s^{(L)}(\mathbf{c}) = \hat{c}[n] * p[n] = \frac{1}{c_{\max}} \sum_{i=0}^{N} c_i p[n - iM], \tag{20}$$

where $p[n] = 0$ when $n \notin [0, \Delta_p - 1]$, and $\max_n\{|p[n]| = 1\}$. Eqs. (19) and (20) show that the discrete-time duration Δ_s depends on the length $N + 1$ of the code-sequence $\mathbf{c}$, the upsampling factor M and the length Δ_p of $p[n]$, as expressed by

$$\Delta_s = MN + \Delta_p. \tag{21}$$

The code and pulse shaper normalization by $c_{\max}$ and $\max_n\{|p[n]|\} = 1$, respectively, ensures that $\max_n\{|\tilde{s}^{(L)}[n]|\} = 1$ when the pulse shaper duration satisfies $\Delta_p \leq M$. This is useful to compare different CE signal waveforms to take into account that, because of technological constraints, the input of each piezoelectric element cannot exceed a maximum value, equal to 1 without restriction of generality. Note that a baseband signal waveform with a (maximum) constant envelope is highly desirable to maximize the energy of the transmitted RF signal, as happens for linear-FM in (18). Thus, to quantify the energy loss with respect to a constant amplitude code, it is common to define the code efficiency η_c as the energy ratio

$$\eta_c = \frac{\sum_{i=0}^{N} |c_i|^2}{(N+1) c_{\max}^2}, \tag{22}$$

which influences the GSNR achievable by a specific code. Analogously, it is possible to define the pulse shaper efficiency η_p, and the overall signal waveform efficiency η_s. Note that $\eta_s = \eta_c \eta_p (N+1)\Delta_p/\Delta_s$, when $\Delta_p \leq M$; in general, this is not the case when $\Delta_p > M$, because of the overlap of the pulse shaper replicas in (19). Indeed, the pulses overlap generates the so called inter-symbol (chip) interference (ISI), which typically produces a higher maximum and higher variability of the signal envelope $|\tilde{s}^{(L)}[n]|$ and, consequently, it contributes to a further efficiency reduction that depends jointly on the code chips $\{c_i\}$ and on the pulse shaper $p[n]$. By means of the discrete-time Fourier transform (DTFT), the transmitted signal spectrum $\tilde{S}^{(L)}(f) = \sum_{n=-\infty}^{+\infty} \tilde{s}^{(L)}[n] \exp(-j2\pi f n T_s)$ is expressed by

$$\tilde{S}^{(L)}(f) = P(f) \sum_{i=0}^{N} c_i e^{-j2\pi f T_s i M} = P(f) C(Mf). \tag{23}$$

Eq. (23) shows that the bandwidth of the complex envelope $\tilde{s}^{(L)}[n]$ is imposed by the pulse shaper spectrum $P(f)$ and, possibly, also by the code spectrum $C(f)$; moreover, higher interpolation factors correspond to higher selectivity of $C(Mf)$, if $C(f)$ shows some selectivity. In the absence of frequency-dependent medium attenuation ($\beta = 0$), the baseband pulse compression output, for an LCE system [(19) and (20)] exploiting a matched filtering, is expressed by

$$\begin{aligned} \tilde{R}_{rs}^{(L)}[n] &= e^{-\alpha|\vec{r}|} \tilde{R}_{ss}^{(L)}[n + n_0] + \tilde{R}_{\mu s}[n] \\ &= \frac{e^{-\alpha|\vec{r}|}}{c_{\max}^2} \sum_{i=0}^{2N} R_{cc}[i] R_{pp}[n + n_0 + NM - iM] + \tilde{R}_{\mu s}[n]. \end{aligned} \tag{24}$$

In (24), $\tilde{R}_{\mu s}[n]$ is associated with the complex envelope of the system noise $\mu[n]$, $R_{pp}[n] = \sum_{m=-\infty}^{+\infty} p^*[m]\, p[m+n]$ is the (non-causal) auto-correlation function of the pulse shaping waveform $p[n]$, and $R_{cc}[n] = \sum_{i=0}^{N} c_i^* c_{i+n-N}$ is the (causal) autocorrelation function of the coding sequence $\mathbf{c}$, with energy $R_{cc}[N]$, assuming that $c_i = 0$ when $i \notin [0, N]$. Moreover, in the presence of frequency-dependent attenuation ($\beta \neq 0$), the matched pulse compression output at the round-trip distance $\vec{r}$ can be expressed by

$$\begin{aligned} \tilde{R}_{rs}^{(L)}[n] &= \tilde{R}_{ss}^{(L)}[n + n_0] * \tilde{h}_{tot}(n, \vec{r}) + \tilde{R}_{\mu s}[n] \\ &= \frac{1}{c_{\max}^2} \sum_{i=0}^{2N} R_{cc}[i] R_{pp_h}(n + n_0 + NM - iM, \vec{r}) + \tilde{R}_{\mu s}[n], \end{aligned} \tag{25}$$

where $R_{pp_h}(n, \vec{r}) = R_{pp}[n] * \tilde{h}_{tot}(n, \vec{r})$, and $\tilde{h}_{tot}(n, \vec{r})$ is the discrete-time baseband complex counterpart of $h_{tot}(t, \vec{r})$. Thus, the effects of a frequency-dependent attenuation will be similar for any LCE system that employs the same

pulse shaping waveform $p[n]$. The LCE design (20) is intended to obtain a coded waveform $s[n]$ such that the correlation function $\tilde{R}_{\mathrm{rs}}[n]$ in (25) [or (24)] approximates a single strong, sharp pulse. Thus, by means of (19), (20), (24), and (25), the first (and minimum) goal is to find a sequence with an autocorrelation function similar to a Kronecker delta (i.e., $R_{\mathrm{cc}}[n] \approx R_{\mathrm{cc}}[N]\delta[n-N]$). This way, assuming the noise $\mu[n]$ and the signal $s[n]$ are almost uncorrelated (i.e., $\tilde{R}_{\mu s}[n] \simeq 0$), by using (22), it is possible to conclude that

$$\tilde{R}_{\mathrm{rs}}[n] \approx \eta_{\mathrm{c}}(N+1)R_{\mathrm{pp}_h}(n+n_0,\vec{r}), \tag{26}$$

and, consequently, the second goal is to design $p[n]$ such that $R_{\mathrm{pp}_h}(n,\vec{r})$ meets the desired specifications. Eq. (25) demonstrates that, independently of the linear code $\mathbf{c}$ that is chosen, the frequency dependence of the attenuation affects the pulse compression output only through an equivalent pulse shaping $p_h[n]$, which is mismatched to the original $p[n]$ employed at the compression stage. This fact can be further appreciated in the frequency domain, in which the compression output spectrum $\tilde{S}_{\mathrm{rs}}(f) = \sum_{n=-\infty}^{+\infty}\tilde{R}_{\mathrm{rs}}[n]\exp(-j2\pi f n T_{\mathrm{s}})$ is characterized by

$$\begin{aligned}\left|\tilde{S}_{\mathrm{rs}}^{(L)}(f)\right| &= \left|\tilde{H}_{\mathrm{tot}}(f,\vec{r})\right||P(f)|^2 S_{\mathrm{cc}}(Mf)\\ &= \left|\tilde{H}_{\mathrm{tot}}(f,\vec{r})\right||P(f)|^2 \sum_{n=0}^{2N}\frac{R_{\mathrm{cc}}(n)}{|c_{\max}|^2}\,\mathrm{e}^{-j2\pi f n M T_{\mathrm{s}}},\end{aligned} \tag{27}$$

where $\tilde{H}_{\mathrm{tot}}(f,\vec{r})$ is the DTFT of the baseband-equivalent system impulse response $\tilde{h}_{\mathrm{tot}}(n,\vec{r})$, $P(f)$ is the DTFT of the pulse shaper $p[n]$, and $S_{\mathrm{cc}}(Mf) = |C(Mf)|^2/c_{\max}^2$ represents the spectrum shaping imposed by the autocorrelation of the (zero-filled) code $\hat{c}[n]$. Eq. (27) highlights that a wider band of $P(f)$ and $C(Mf)$ could guarantee a sharper compression output $\tilde{R}_{\mathrm{rs}}^{(L)[n]}$ (i.e., higher axial resolution), if the medium frequency response $\tilde{H}_{\mathrm{tot}}(f,\vec{r})$ is not too frequency-selective.

IV. Huffman Coding

In 1962, Huffman [39] presented a family of complex discrete sequences $\mathbf{c}_{\mathrm{H}} = [c_{\mathrm{H},0}, c_{\mathrm{H},1}, \ldots, c_{\mathrm{H},N}]$ with autocorrelation functions $R_{c_{\mathrm{H}}c_{\mathrm{H}}}[n]$ expressed by

$$R_{c_{\mathrm{H}}c_{\mathrm{H}}}[n] = \begin{cases}\displaystyle\sum_{i=0}^{N}|c_{\mathrm{H},i}|^2, & n = N\\ \displaystyle -\frac{R_{c_{\mathrm{H}}c_{\mathrm{H}}}[N]X^{-N}}{1-X^{-2N}}, & n = 0, 2N\\ 0, & \text{elsewhere,}\end{cases} \tag{28}$$

where X is a design parameter and, by means of (28), it corresponds to our desired Kronecker delta target, except for $n = 0$ and $n = 2N$. Huffman demonstrated that a sequence $\mathbf{c}_{\mathrm{H}}$ has the autocorrelation function expressed by (28), if its Z-transform

$$C_{\mathrm{H}}(z) = \sum_{i=0}^{N} c_{\mathrm{H},i}z^{-i} = c_{\mathrm{H},0}\prod_{k=1}^{N}(1-z^{-1}z_k), \tag{29}$$

has all the zeros $\{z_k\}_{k=1,\ldots,N}$ that are spaced at equal angular intervals in the z-plane and lie in one of two origin-centered circles, with radii X and $1/X$, as expressed by

$$z_k = \begin{cases} Xe^{j2\pi k/N}, & \text{if the } k\text{th zero has radius } X\\ X^{-1}e^{j2\pi k/N}, & \text{if the } \boldsymbol{k}\text{th zero has radius } 1/X.\end{cases} \tag{30}$$

Thus, the code MSR ($\mathrm{MSR_c}$) is expressed by [15]

$$\mathrm{MSR_c} = \left|\frac{R_{c_{\mathrm{H}}c_{\mathrm{H}}}[N]}{R_{c_{\mathrm{H}}c_{\mathrm{H}}}[2N]}\right| = X^N - X^{-N}. \tag{31}$$

Summarizing, a Huffman sequence can be found by implementing the following steps [40]:

1) Fix the code length to $N+1$.
2) Choose X that determines the radius of the two origin-centered circles.
3) For each zero z_k, $k = 1, \ldots, N$, choose which of the two origin-centered circles it belongs to.
4) Once all the N zeros $\{z_1, \ldots, z_N\}$ are chosen, compute the $N+1$ polynomial coefficients $\{c_{\mathrm{H},0}, \ldots, c_{\mathrm{H},N}\}$.

The third step of the described procedure highlights that, once the two parameters N and X are selected [e.g., by fixing the maximum sequence length and the $\mathrm{MSR_c}$ in (31)], there are 2^N different sequences with the same autocorrelation function expressed by (28), each one characterized by its own efficiency η_{c} [see (22)].

Interestingly, although not widely acknowledged, Ackroyd proposed in [27] a method to assign the appropriate circle to each zero to maximize the efficiency η_{c} of the code. This is done by approximating the phase constraint imposed by the Schroeder rule [41] as

$$\arg C_k = \arg C_0 - \pi k^2/(N+1) + \zeta k, \quad k \in [0, N], \tag{32}$$

where $C_k = C(kf_{\mathrm{s}}/(N+1))$, and $\mathbf{C} = [C_0, \ldots, C_k, \ldots, C_N]$ is the $(N+1)$ discrete Fourier transform (DFT) of the sequence $\mathbf{c}_{\mathrm{H}} = [c_{\mathrm{H},0}, \ldots, c_{\mathrm{H},i}, \ldots, c_{\mathrm{H},N}]$, and $\arg C_0$ and ζ can be chosen arbitrarily. In [27], Ackroyd proposed a method to approximate (32) for Huffman codes: if a zero z_k is outside the unit circle in the z-plane (i.e., it belongs to the circle with radius $1/X$, if $0 < X < 1$), it will contribute to the phase spectrum by a smooth phase transition of $+\pi$ centered at the digital frequency k/N; otherwise its contribution will be a smooth phase transition of $-\pi$. Thus, an approximation of $\pm\pi$ to the desired phase spectrum can be represented by a piece-wise constant function with $\pm\pi$ steps centered at the zero location belonging either to the

circle outside or the circle inside the unit circle. Moreover, to avoid the numerical approximation errors associated to polynomial root-finding algorithms in (29), which may be significant for high values of the sequence length $(N+1)$, it is possible to implement step 4 by inverting (29) on the $(N+1)$ DFT grid,

$$c_{\mathrm{H},i} = \frac{1}{N+1}\sum_{k=0}^{N} C_{\mathrm{H}}(e^{-j(2\pi/(N+1))ik})e^{j(2\pi/(N+1))ik}, \quad i = 0,\ldots,N,$$

as suggested in [27] and better described in [42].

A. Huffman Coding Design Criteria for Medical Ultrasound Applications

Figs. 4 and 5 show the normalized code envelope $|c_{\mathrm{H},i}|/c_{\mathrm{H}_{\max}}$ and the ambiguity function $\tilde{\chi}_{\mathrm{ss}}(n, f_{\mathrm{d}})$, respectively, of a Huffman code-sequence with length $N = 64$, obtained by the Ackroyd technique when $f_{\mathrm{s}} = 100$ MHz, and $M = 16$. Although the procedure that has been used in this paper, and that was proposed in [27], consists of the search of the Huffman zero pattern that maximizes the code efficiency η_{c}, it also provides a sequence with a ridge-like ambiguity function. This makes the code robust to the Doppler frequency shifts in (15) introduced by the flow of blood particles, which is highly desirable in ultrasound pulsed-Doppler applications. The explanation for this property is that the Schroeder phase constraint in (32) is the phase of a chirp modulation (linear-FM), which is known to be characterized by a ridge-like ambiguity function. This fact is also evident from [25], in which the goal was exactly to find a Huffman zero-pattern that produces a sequence with an energy distribution that approximates that of linear-FM. Also for this reason, linear-FM is a natural candidate for a performance comparison with the proposed Huffman CE, as will be detailed in Section V.

Leveraging on the analytical framework derived in Section III-A, it is also possible to easily describe the Huffman code effect on the pulse compression output in the presence of a frequency-dependent attenuating medium. Indeed, by means of (28), and ignoring the noise cross-correlation contribution, (25) becomes

$$\begin{aligned}\tilde{R}_{r_{\mathrm{H}}s_{\mathrm{H}}}[n] = \eta_{\mathrm{c}}(N+1)\Big[& R_{\mathrm{pp}_h}(n+n_0,\vec{r}) \\ & + \frac{1}{\mathrm{MSR}_{\mathrm{c}}} R_{\mathrm{pp}_h}(n+n_0+NM,\vec{r}) \\ & + \frac{1}{\mathrm{MSR}_{\mathrm{c}}} R_{\mathrm{pp}_h}(n+n_0-NM,\vec{r})\Big],\end{aligned} \tag{33}$$

where $\tilde{r}_{\mathrm{H}}[n]$ and $\tilde{s}_{\mathrm{H}}[n]$ are the received and transmitted signal associated to the Huffman sequence $\mathbf{c}_{\mathrm{H}}$. Eq. (33) explains that when $\beta = 0$, i.e., when $R_{\mathrm{pp}_h}(n,\vec{r}) = e^{-\alpha|\vec{r}|}R_{\mathrm{pp}}[n]$, and if the pulse shaper autocorrelation side lobes are properly designed, then the MSR of the overall system depends only on $\mathrm{MSR}_{\mathrm{c}}$, which is imposed by the selection of the code length $N+1$ and the parameter X by (31). Conversely, when $\beta \neq 0$, it is important to consider the degradation on the overall MSR introduced by the side lobes of $R_{\mathrm{pp}_h}(n,\vec{r})$ [i.e., the mismatch imposed by $\tilde{h}_{\mathrm{tot}}(n,\vec{r})$]. Moreover, for a fixed code efficiency η_{c} (maximized by the Ackroyd method), the axial resolution and the GSNR depend on the width and the (maximum) amplitude, respectively, of the autocorrelation function $R_{\mathrm{pp}_h}(n,\vec{r})$. For this reason, it is important to design the pulse shaper $p[n]$ such that the practical bandwidth B of the coded waveform $\tilde{s}_{\mathrm{H}}[n]$, i.e., $P(f)$, is within the frequencies that the piezoelectric transducer can achieve, and such that the correlation function $R_{\mathrm{pp}_h}(n,\vec{r})$ has a narrow main lobe with a high peak and, possibly, low side lobes for the set of round-trip distances $\{\vec{r}\}$ of interest.

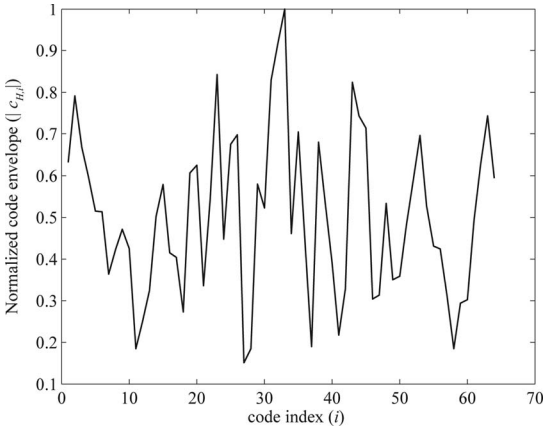

Fig. 4. Envelope of the Huffman code ($N = 64$) obtained by [27].

To confirm this analysis, this section shows the pulse compression performance of three Huffman waveforms; all of them were designed by the Ackroyd method in [27] using $N = 48$, $M = 21$, $X = 0.825$, $f_{\mathrm{s}} = 100$ MHz, but each of them uses an FIR pulse $p[n]$ with a different value of the -3-dB bandwidth, $B_{-3\mathrm{dB}}$. Specifically, the three wave-

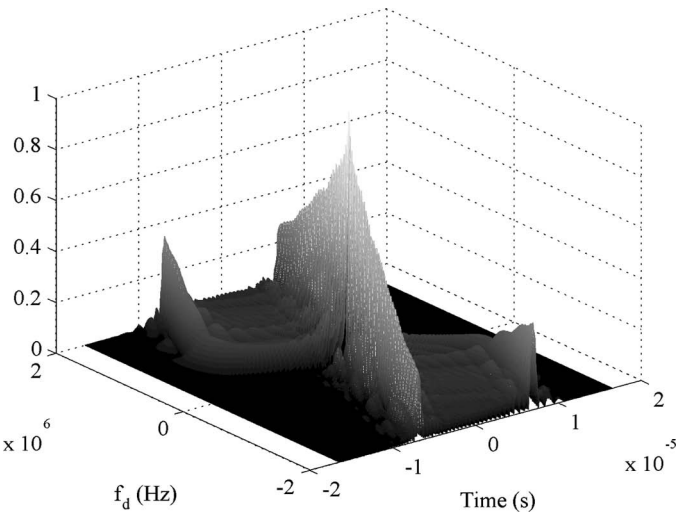

Fig. 5. Ambiguity function of the Huffman code ($N = 64$) obtained by [27].

forms are expressed by $p[n] = w_{\rm cb}[n]h_{\rm bw}[n]$, where $h_{\rm bw}[n]$ is the FIR impulse response of an ideal brick-wall low-pass filter with the same baseband cut-off frequency $f_{\rm c} = 1.3$ MHz, and different orders $\Delta_{\rm p} - 1 = \{54, 78, 100\}$; $w_{\rm cb}[n]$ is the Chebyshev time-domain window [43], expressed by

$$w_{\rm cb}[n] = \mathfrak{F}_{\Delta_{\rm p}}^{-1}\left((-1)^{\nu} \frac{\cos\left[\Delta_{\rm p}\cos^{-1}\left[\varepsilon\cos\left(\pi\frac{\nu}{\Delta_{\rm p}}\right)\right]\right]}{\cosh\left(\Delta_{\rm p}\cosh^{-1}(\varepsilon)\right)} \right), \quad (34)$$

where $n \in [0, \Delta_{\rm p}]$, $\varepsilon = \cosh\left(1/\Delta_{\rm p}\cosh^{-1}(10^{\gamma})\right.$, $\gamma = 5.25$, $\mathfrak{F}_{\Delta_{\rm p}}^{-1}$ is the $\Delta_{\rm p}$-point inverse DFT, and $\nu = 0, \ldots, \Delta_{\rm p}$ is the discrete frequency index. The three Chebyshev windows with different lengths $\Delta_{\rm p} = \{55, 79, 101\}$ induce, at RF, three different overall -3-dB bandwidths, $B_{-3{\rm dB}} = \{3.6, 2.7, 2.3\}$ MHz, respectively. Note that, to contrast the tails overlapping of the spectrum $\tilde{S}^{(L)}(f)$ induced by the RF modulation at $f_0 = 4$ MHz, all three baseband brick-wall filters $h_{\rm bw}[n]$ have been designed with frequency side lobes at least -105 dB from the main lobe peak, when $|f| > 3$ MHz.

In the simulation, the transducer spatial impulse response $h_{\rm s}(t, \vec{r})$ in (4) is neglected, and the presence of a frequency-dependent attenuating medium is considered by means of (5), with an attenuation coefficient $\beta = 0.7$ dB/(MHz·cm) that, according to [44], can adequately model liver behavior. The transducer is modeled by the frequency response shown in Fig. 6, which corresponds to the same discrete-time temporal impulse response $h_{\rm t}[n] = h_{\rm t}(nT_{\rm s})$ used in [8] and [16], and it was obtained by experimental measures on a mechanically rotating transducer with central frequency $f_{\rm o} = 4$ MHz and bandwidth $B = 2.6$ MHz. Moreover, by means of (5), Fig. 6 also shows the normalized frequency response $|H_{\rm att}(f, \vec{r})|/|H_{\rm att}(0, \vec{r})|$ of the attenuating medium for a set of distances $|\vec{r}|/2 = \{5, 15, 30\}$ cm.

Fig. 7 shows the GSNR performance for the three different pulse shapers, whereas Fig. 8 shows the pulse compression output when either $\beta = 0$ or $\beta = 0.7$ dB/(MHz·cm) at two scattering distances $|\vec{r}|/2 = 15$ cm and $|\vec{r}|/2 = 30$ cm. The two figures highlight that the pulse shaping waveform $p[n] = w_{\rm cb}[n]h_{\rm bw}[n]$ with the widest $B_{-3{\rm dB}}$ bandwidth of $P(f)$ provides the best GSNR at high scattering distances, and the worst GSNR at short distances; moreover, Fig. 8(a) shows that, in frequency-dependent attenuating tissues, the pulse shaper with widest bandwidth has worse contrast resolution, caused by the $R_{{\rm pp}_h}(n, \vec{r})$ side lobes. This phenomenon, which is also moderately observable in Fig. 8 when $\beta = 0$, produces a spectrum floor of spurious components on the RF signal. These undesired components, which increase with the bandwidth $B_{-3{\rm dB}}$ of $P(f)$, are also present at low frequencies, where the frequencies are less attenuated in a frequency-dependent attenuating tissue (see Fig. 6). Thus, for increasing propagation distances in the tissue, these spurious low-frequencies become increasingly more significant with respect to the RF spectrum of the desired pulse compression

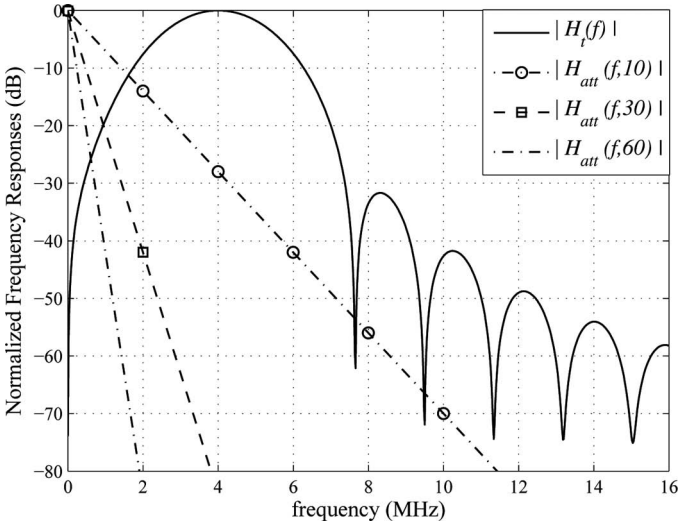

Fig. 6. Frequency response of the mechanically rotating transducer in [8] and [16]. Dashed lines: the normalized frequency response of the medium at three different distances $|\vec{r}|/2 = \{5, 15, 30\}$ cm.

output at 4.0 MHz. These spurious low-frequencies are responsible for a higher side lobe floor in the time domain.

Summarizing, in the absence of frequency-dependent attenuation, and with the Ackroyd design, (properly designed) pulse shapers with wider bandwidth provide only better axial resolution, whereas the MSR and GSNR depend on the specific code that is used. However, in the presence of frequency-dependent attenuation the MSR and GSNR are also influenced by the bandwidth of the pulse shaping waveform through the correlation function $R_{{\rm pp}_h}(n, \vec{r})$ in (33). Thus, taking into account the penetration depth of the diagnostic region of interest, the pulse shaping waveform must be designed by trading high robustness to frequency-dependent attenuating media, for both MSR and GSNR. For instance, the pulse shaping waveform with the widest bandwidth, i.e., $B_{-3{\rm dB}} =$

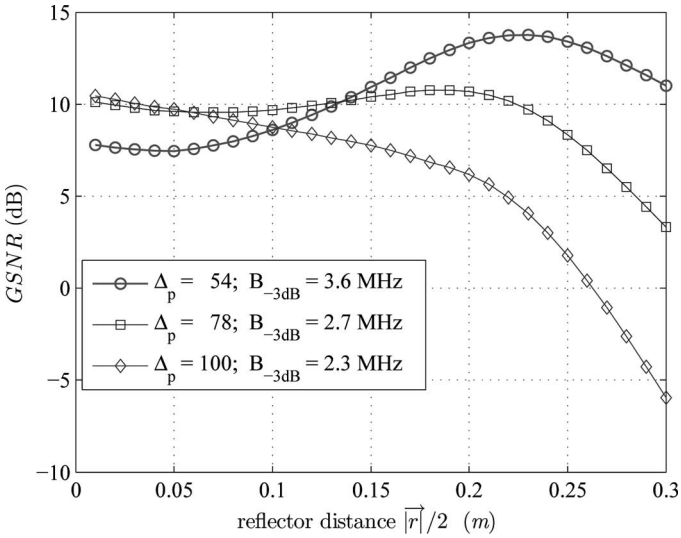

Fig. 7. Signal-to-noise ratio gain (GSNR) performance for three different -3-dB bandwidth pulse shaping designs.

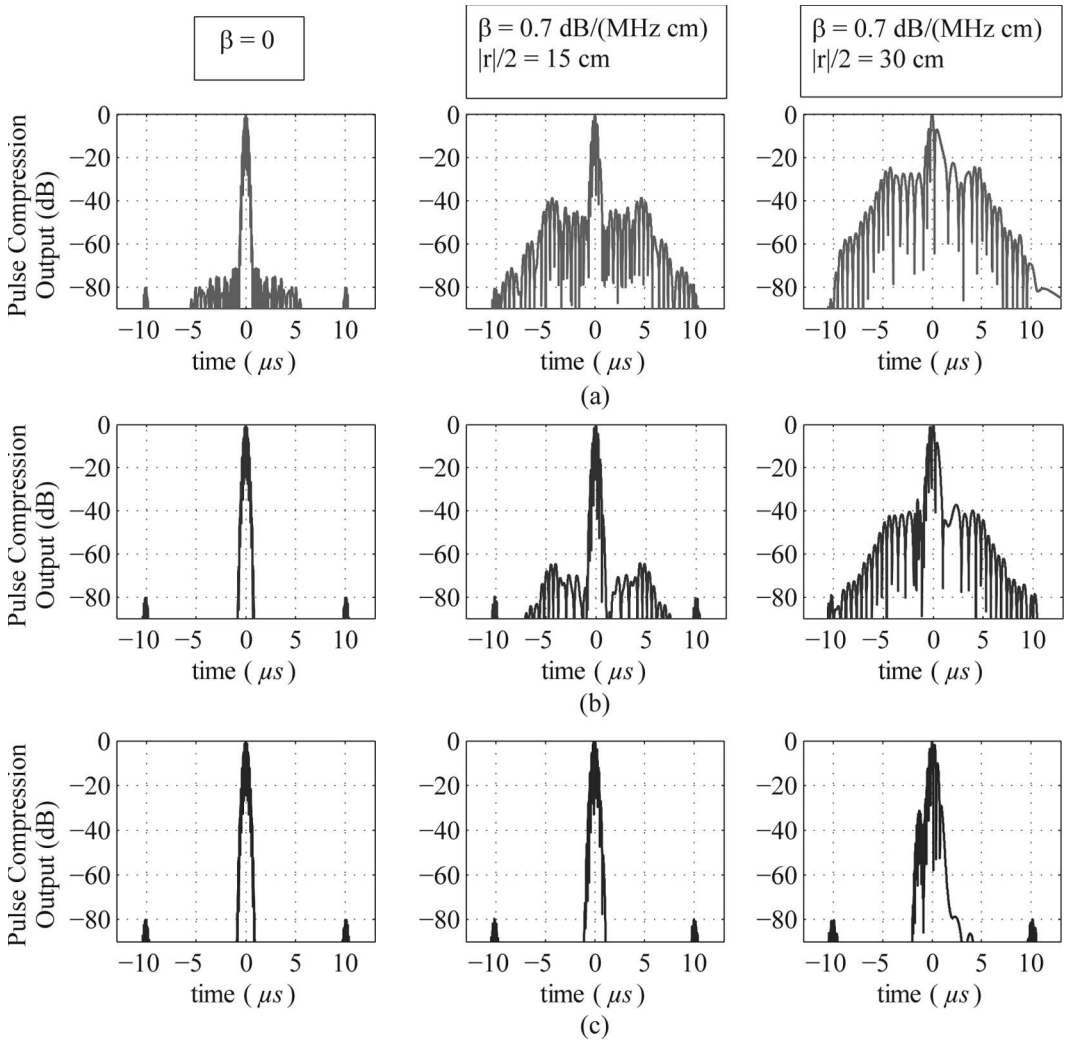

Fig. 8. Pulse compression output for three pulse shapers (in each row): (a) $B_{-3\mathrm{dB}} = 3.6$ MHz; (b) $B_{-3\mathrm{dB}} = 2.7$ MHz; and (c) $B_{-3\mathrm{dB}} = 2.3$ MHz.

3.6 MHz, must be chosen to trade contrast resolution for higher GSNR and penetration depth. On the contrary, the smallest bandwidth, i.e., $B_{-3\mathrm{dB}} = 2.3$ MHz, must be chosen to trade GSNR for maximum axial and contrast resolution (MSR).

Another important aspect is that the upsampling factor M of (19) affects both the signal duration $\Delta_\mathrm{s} T_\mathrm{s}$ [see (21)] and the side lobe distance, as summarized by (33). Although a high side lobe separation in time is not particularly useful in medical applications, the maximum signal duration $\Delta_\mathrm{s} T_\mathrm{s}$ is typically constrained in ultrasound systems, because of the damping effect of the piezoelectric elements, and also to avoid a too-large dead-zone in the final B-mode image. For this reason, when $\Delta_\mathrm{p} \ll MN$ in (21), because the transmitted signal length $T = \Delta_\mathrm{s} T_\mathrm{s} \approx \mathrm{MNT_s}$ is fixed by the ultrasound transducer, a choice of the parameter M (or N) would correspond to fix the other parameter N (or M) by $N = Tf_\mathrm{s}/M$ (or $M = Tf_\mathrm{s}/N$). To optimize the choice of the pair of parameters (M, N) achievable with the CE technique, it is possible to define two different criteria:

1) the ISI-free criterion (IFC);
2) the exhaustive-optimal criterion (EOC).

The IFC is based on the observation that the most significative samples of a pulse shaping waveform $p[n]$ with bandwidth B are approximately equal to $\lceil f_\mathrm{s}/B \rfloor$ and thus, to avoid ISI in $\tilde{s}_\mathrm{H}[n]$, it is possible to choose $M \approx \lceil f_\mathrm{s}/B \rfloor$, as proposed in [45]. However, this simple criterion does not take into account other significant aspects, as will be clarified. Indeed, for a fixed signal duration $\Delta_\mathrm{s} T_\mathrm{s}$, a smaller value of M would allow the use of higher values of N and, thus, a longer sequence $\mathbf{c}_\mathrm{H}$ that, in general, gives better chances to find a sequence with high efficiency η_c. On the other hand, the EOC determines the best choice of M by evaluating the GSNR for all of the possible values of N such that $M = Tf_\mathrm{s}/N$ and, thus, it jointly considers the code efficiency η_c in (22) and the overall signal efficiency η_s. To clarify this point, Figs. 9 and 10 compare, respectively, the baseband magnitude $|\tilde{s}_\mathrm{H}[n]|$ and the auto-correlation magnitude $\left|\tilde{R}_{s_\mathrm{H} s_\mathrm{H}}[n]\right|$ for different values of M and N, with $\mathrm{MSR_c} = 80$ dB, $f_\mathrm{s} = 100$ MHz, $T \approx 10$ μs, the same

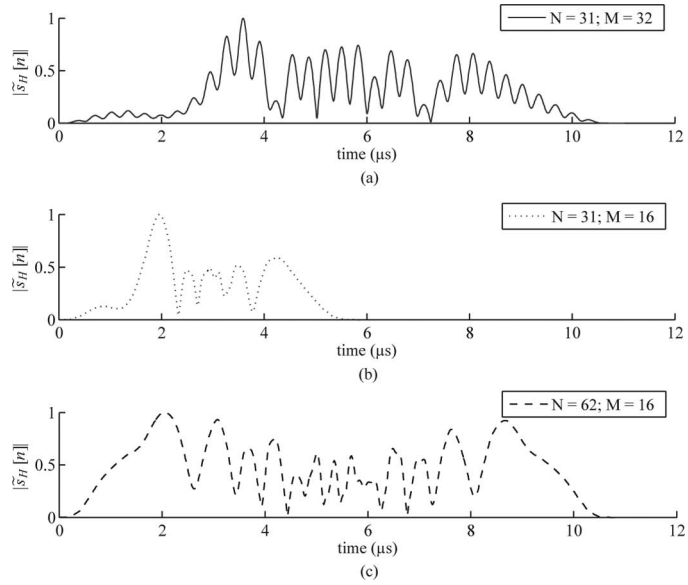

Fig. 9. (a)–(c) Complex envelopes of the transmitted signal $s[n]$ for different values of N and M.

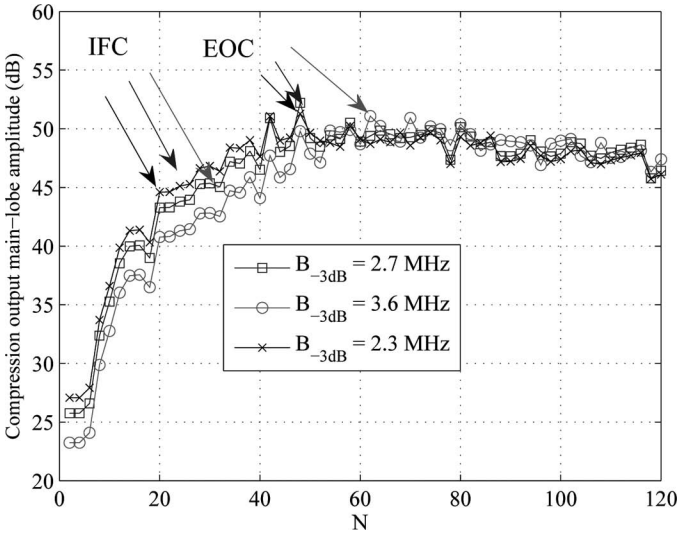

Fig. 11. Main lobe amplitude of $\tilde{R}_{s_H s_H}$ for different values of N (T = 10 μs, f_s = 100 MHz, $\mathrm{MSR_c}$ = 80 dB, $M = \lceil Tf_s/N \rceil$, Ackroyd design [27]).

Chebyshev pulse shaping waveform $p[n] = w_{\mathrm{cb}}[n]h_{\mathrm{bw}}[n]$, and Huffman codes $\mathbf{c}_{\mathrm{H}}$ designed by the Ackroyd method. Specifically, from Figs. 9 and 10, it is possible to understand that, for $N = 31$, a smaller value of M produces a shorter signal $\tilde{s}_{\mathrm{H}}[n]$, but also a smaller main lobe amplitude that induces a worse GSNR. Moreover, by comparing the signals in Fig. 9(a) and 9(c) it is evident that, although they have the same duration $\Delta_s = NM + \Delta_p$ (21), the one in Fig. 9(c) provides a higher main lobe amplitude (better GSNR), as shown in Fig. 10.

Fig. 11 shows the main lobe amplitude (i.e., the signal energy) of the autocorrelation $\tilde{R}_{s_H s_H}[n]$ using the Ackroyd method, for different values of N when $T = 10$ μs, f_s = 100 MHz, $\mathrm{MSR_c}$ = 80 dB, and $M = \lceil Tf_s/N \rceil$, for all three pulse shaping functions used for Figs. 7 and 8. The figure highlights how the EOC would improve the GSNR performance with respect to the IFC; however, how the ISI affects the autocorrelation main lobe amplitude depends on the specific code-sequence, $\mathbf{c}_{\mathrm{H}}$.

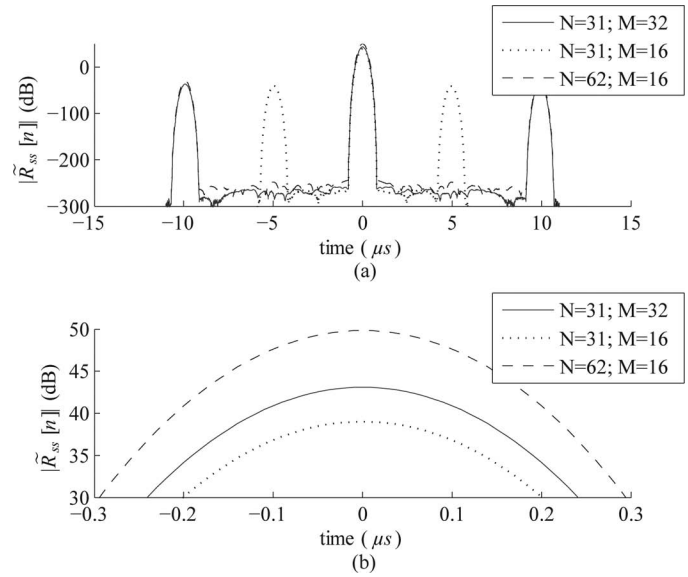

Fig. 10. (a) Baseband auto-correlation functions for different values of N and M. (b) Magnification and detail of the main lobe.

Fig. 12 shows the code ambiguity function and the pulse compression output at a scattering distance $|\vec{r}|/2$ = 30 cm, with β = 0.7 dB/(MHz·cm), for two different transmitted waveforms obtained by Huffman coding with $X = 0.825$ and $(M, N) = (21, 48)$. Specifically, for the first waveform, the Huffman code is obtained by the Ackroyd procedure described in [27], whereas the second one is obtained by a random choice of the zero locations on the two origin-centered circles with radius X and $1/X$. Fig. 12(a) shows that, because it uses the Ackroyd design, the first waveform provides a quasi-ridge-like ambiguity function whereas the second signal, because of the random choice of the zeros location, exhibits in Fig. 12(c) an ambiguity function with a quasi-thumbtack shape. On the contrary, Figs. 12(b) and 12(d) show that the (peak-normalized) pulse compression output $\tilde{R}_{r\varphi}[n] = \tilde{\chi}_{r\varphi}(n, 0)$ of the two signals assume similar values (also in the presence of frequency-dependent attenuating media), except for some slight differences of the shape (i.e., not of the maximum amplitudes) of the side lobes. This confirms that the ambiguity function does not affect the pulse compression performance of the overall system and should not be used as a design criterion for CE techniques, unless designing for pulse-Doppler applications.

V. Coding Performance

This section, by focusing only on the correlation results, evaluates the output of the matched filter ($\psi[n] = s_{\mathrm{H}}[n]$) for the proposed Huffman waveform design. The next section will more practically evaluate the system performance by taking into account the tissue attenuation, as

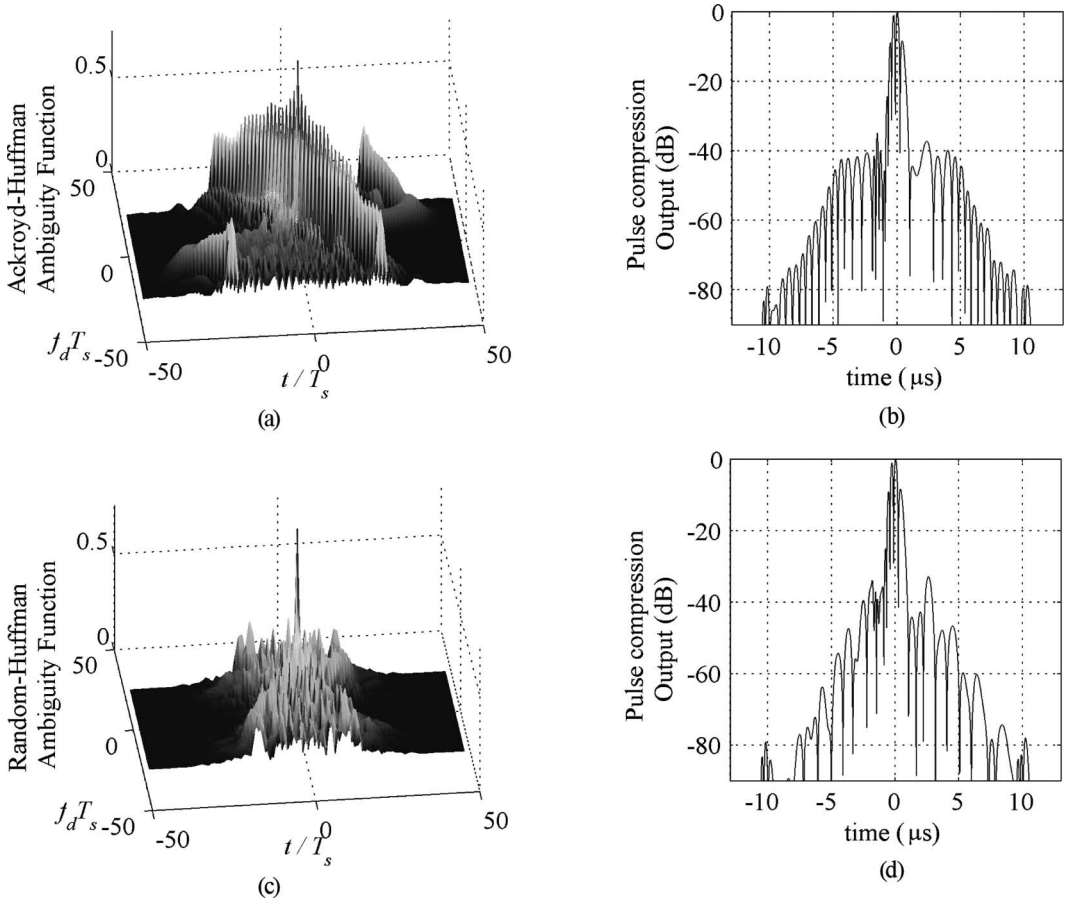

Fig. 12. Ambiguity function and pulse compression output comparison for different Huffman codes: (a) Ackroyd [27] design. (b) Random choice of the zeros in the two circles of (30).

well as the transducer geometry and a specific beamforming technique. The pulse shaping waveform $p[n] = h_{\rm bw}[n]$ $w_{\rm cb}[n]$ has been designed as a 79-taps brick-wall FIR filter $h_{\rm bw}[n]$ with $B_{-3{\rm dB}} = 2.7$ MHz, and a Chebyshev window $w_{\rm cb}[n]$ employing $\gamma = 5.25$ [see the definition of ε in (34)]. As suggested by the EOC criterion (see Fig. 11), it has been chosen a Huffman code with length $N = 48$ and upsampling factor M= 21, which corresponds to a signal duration $T \approx 10$ μs at $f_{\rm s} = 100$ MHz. Note that the upsampling factor M has little influence on the signal bandwidth when the code exhibits quasi-Kronecker-delta autocorrelation [see (23)], as for Huffman codes. The Huffman code has been generated by the Ackroyd approach [27], setting in (31) the radius X that guarantees ${\rm MSR_c} =$ 80 dB. The linear-FM code proposed in [16] is considered for the first comparison, where, to reduce the Fresnel distortion, the signal has a bandwidth of 7.8 MHz before the transducer, and it is tapered by a Tukey window. Moreover, to minimize the main lobe width for a specified constant side lobe level, as deeply investigated in [38], the linear-FM system has been optimized in [16] employing a mismatched pulse compression waveform $\psi[n] = s^{(c)}[n]$ $w_{\rm dc}[n]$, where $w_{\rm dc}[n]$ is a Dolph–Chebyshev time-domain window. This way, the linear-FM coding is characterized by a higher MSR and it becomes more suited to medical applications. For a second challenging comparison, this section employs the double-transmission complementary Golay approach in [14], which is an optimal solution (that penalizes the frame rate), because a complementary Golay code, $\mathbf{c}_{\rm G}$, can guarantee the ideal autocorrelation function $R_{c_{\rm G}c_{\rm G}}[n] = R_{c_{\rm G}c_{\rm G}}[N]\delta[n-N]$ in (25). Specifically, the complementary Golay code has been generated as in [46], by using a matched filtering pulse compression and a transmitted signal $s[n]$ with duration $T = 10$ μs. The signal in [46], characterized by a constant amplitude, is very easy to generate and it can be expressed by (20) using $N = 20$, M $= 50$, and a rectangular pulse shaping waveform $p[n] = 1$, $n \in [0, M-1]$, as in [16].

Note that, for this classical Golay CE formulation, the value of M influences the signal bandwidth through the duration of the rectangular pulse shape $p[n]$. Specifically, $P(f)$ is a sinc$(\cdot)$ function with first zero location at $f_{\rm s}/M =$ 2 MHz and $B_{-3{\rm dB}} \simeq 1.78$ MHz. Thus, because of its lower frequency support, taking into account (27) and (25), this code will exhibit a wider main-pulse compression output (worsen axial resolution) with respect to both the proposed Huffman code and the linear-FM. To consider a comparable bandwidth $B_{-3{\rm dB}}$, the value of M should be reduced approximately by a factor of three (e.g., $M = 17$).

In this view, and also to better highlight how the pulse shaping waveform $p[n]$ affects the pulse compression, the third comparison considers the performance of comple-

TABLE I. SIGNAL-TO-NOISE RATIO GAIN (GSNR), MAIN-TO-SIDE LOBE RATIO (MSR), AND AXIAL RESOLUTION COMPARISON FOR DIFFERENT CODED-EXCITATION TECHNIQUES [RESULTS EXTRACTED FROM FIG. 13(B)].

	Huffman	Tapered linear FM [32]	Golay with $p_{\text{rect}}[n]$ [10]	Golay with $p_{\text{rect}}[n]$
GSNR (dB)	10.0	10.6	17.7	13.3
MSR (dB)	80	65	∞	∞
Axial resolution (mm)	1.3	1.2	1.7	1.3

mentary Golay codes using $N = 26$ and $M = 38$ according to the IFC criterion, and the same pulse shaping waveform $p[n] = w_{\text{cb}}[n]h_{\text{bw}}[n]$ employed for the Huffman code, which also imposes the same bandwidth. However, note that such a pulse shaper sacrifices the easy generation properties of classical Golay coding approaches by introducing a non-constant envelope.

Fig. 13 compares the baseband matched filter output $\tilde{R}_{r_{\text{H}}s_{\text{H}}}[n]$ of the Huffman code, with the mismatched filter output of a 10-μs linear-FM code [16] and with the two double-transmission Golay approaches described previously, in the absence [Fig. 13(a)] and in the presence [Fig. 13(b)] of the transducer impulse response $h_{\text{t}}[n]$.

The transducer has been modeled with the same temporal impulse response $h_{\text{t}}[n]$ employed in [8], [16] with central frequency equal to 4 MHz and 65% of fractional-bandwidth, as shown in Fig. 6. As is well known, Fig. 13 highlights that the Golay approaches provide an MSR that differs from the theoretical values $+\infty$, only because of numerical approximation errors. Moreover, although they are characterized by the best GSNR, actually 3 dB of their GSNR gain is only due to the double transmission, with duration $2T$. Specifically, rectangular pulse shaped Golay (R-Golay) provides a very high GSNR, but also a noticeably worse axial resolution. On the contrary, the Chebyshev-shaped Golay (C-Golay) approach provides quite the same GSNR of the Huffmann codes, plus a 3 dB gain obtained by the double transmission; moreover, it is characterized by exactly the same axial resolution of the Huffman technique, as predicted by (25) and (28) for quasi-ideal LCE. For figure clarity, the C-Golay plot is represented only by square-markers, because, as highlighted by (25), C-Golay and Huffman codes have an identical main lobe because they employ the same pulse-shaper $p[n]$. Huffman coding has, by design, MSR = 80 dB, which is much better than the MSR = 65 dB of the tapered linear-FM (TLF) approach, whereas it is characterized by approximately the same GSNR and by a small penalty in terms of axial resolution. This fact is summarized in Table I, where the −20-dB axial resolution has been measured according to the approach in [37]. Note that the better performance provided by the Golay coding scheme in the absence of frequency-dependent attenuation requires a double transmission that reduces by 50% the B-mode frame rate and may also induce motion artifacts.

Fig. 13 plots the baseband results obtained using the complex envelope $\tilde{s}_{\text{H}}[n]$, although Fig. 1 shows that, to generate the ultrasound signal $s(t)$, the complex envelope signal $\tilde{s}[n]$ must first be modulated at RF and then digital-to-analog converted. In this view, Figs. 14 and 15 show the pulse compression outputs of the Huffman and the Chebyshev-shaped Golay coding, respectively, in the presence of RF modulation, quantization (6-, 8- and 12-bits), and employing the same transducer used for Fig. 13(b). For figure clarity, TLF and the rectangular-shaped Golay quantization are not illustrated; indeed, modulation and quantization do not significantly degrade the TLF pulse compression performance, and rectangular-shaped Golay codes are very easily generated without any performance loss.

Figs. 14 and 15 also highlight that RF modulation slightly degrades the pulse compression because of the aliasing of the frequency side lobes of the pulse-shaper frequency response. Moreover, although 12-bit and 8-bit quantization do not significantly degrade the pulse compression performance, providing an MSR almost equal to 80 dB, as in the baseband Huffman code design, 6-bit quantization induces a pronounced degradation with an MSR performance similar to TLF.

Note that for LCE approaches exploiting matched pulse compression, the axial resolution depends only on the pulse shaping waveform $p[n]$ in (20), whereas for the TLF, it mostly depends on the mismatched pulse compression waveform $\psi_{\text{C}}[n]$. Thus, the results in Table I refer to the mismatched pulse compression waveform $\psi_{\text{C}}[n] =$

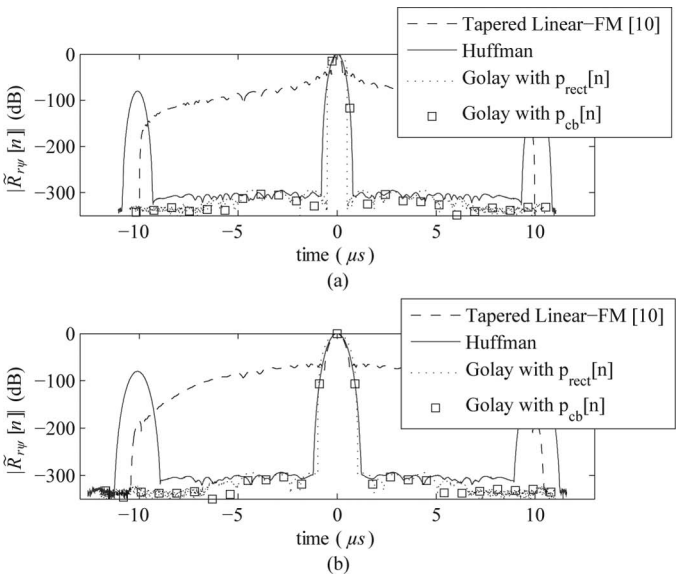

Fig. 13. Pulse compression performance (a) in the absence and (b) in the presence of the transducer impulse response $h_{\text{t}}[n]$.

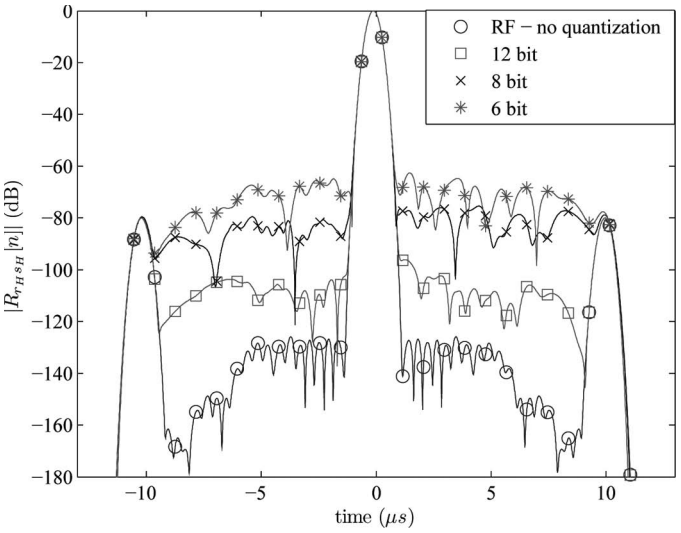

Fig. 14. Pulse compression performance for RF Huffman transmitted signals with quantization.

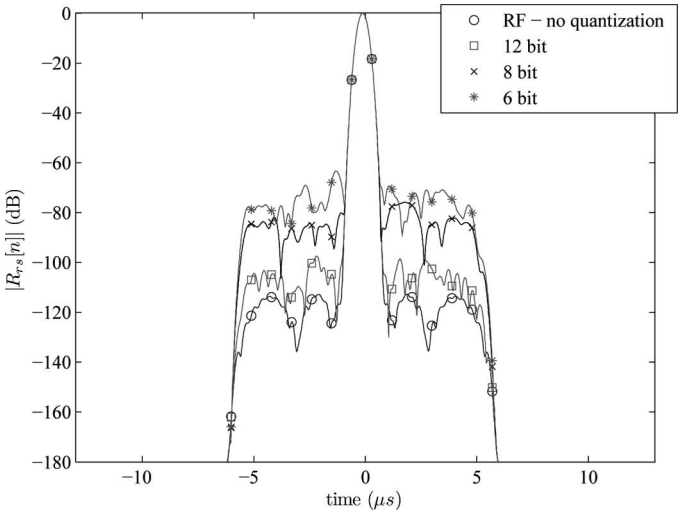

Fig. 15. Pulse compression performance for RF Chebyshev-shaped Golay transmitted signals with quantization.

$s^{(c)}[n]w_{\mathrm{dc}}[n]$ that Misaridis [16] showed to be the appropriate trade-off between axial resolution and side lobe levels (i.e., MSR). However, to be as fair as possible, Table II also shows the TLF performance for different frequency side lobes attenuation of the Dolph–Chebyshev (DC) window $w_{\mathrm{dc}}[n]$.

For instance, by fixing the same axial resolution of 1.3 mm that is obtained for Huffman CE, Table II shows that it is possible in this way to slightly improve the MSR to 70 dB, which is, however, still well below the 80 dB that was imposed by design for the Huffman CE.

VI. Ultrasound Imaging With Huffman Coding

Coded-excitation techniques can be effectively compared by a B-mode imaging approach. To this end, ultrasound imaging simulations were performed by exploiting the same equation used by Field II [28] to model the probe, the tissue, and the transmission technique. As in Section V, each piezoelectric element is modeled by a filter with center nominal frequency $f_0 = 4$ MHz, fractional-bandwidth equal to 65%, and temporal impulse response equal to that one used in Section V.

Fig. 16 shows the GSNR performance in a frequency-dependent attenuating medium [$\beta = 0.7$ dB/(MHz·cm)] for Huffman, TLF, and Golay coding for different scattering distances $|\vec{r}|/2$. Specifically, the Huffman approach employs $(M, N) = (21, 48)$ and a Chebyshev pulse shaping waveform $p[n]$ with $B_{-3\mathrm{dB}} = 2.7$ MHz. This way, the Huffman GSNR performance shown in Fig. 16 are the same that are displayed with square markers in Fig. 7. Moreover, the Golay approach employs both $(M, N) = (50, 20)$ and $(M, N) = (38, 26)$ with rectangular and Chebyshev shaping, respectively, as detailed in Section IV. Fig. 16 highlights that, except for the difference of 3 dB caused by the double transmission, the Huffman and the C-Golay approaches have quite the same GSNR performance. This confirms the analytical derivations in Section III, which has shown that the frequency-dependence of the attenuation affects the system performance only through the equivalent pulse shaping function $p_h[n]$, independently of the specific linear code that is used. Moreover, Fig. 16 also highlights that the R-Golay technique gives the best results in terms of GSNR, but, as it will be clarified in the following simulation results, in some circumstances it can-

TABLE II. Axial and Contrast Resolution of Tapered Linear FM [16] With Different Mismatching Windows.

$w_{\mathrm{dc}}[n]$ frequency side lobe	MSR (dB)	Axial resolution (mm)
−10	55	1.0
−60	65	1.2
−100	70	1.3
−200	70	1.6

MSR = Main-to-side lobe ratio.

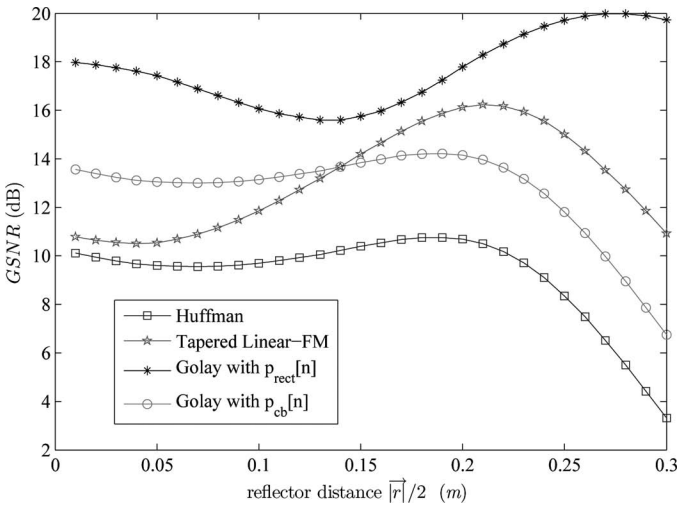

Fig. 16. Signal-to-noise ratio gain (GSNR) performance comparison in frequency-dependent attenuating medium.

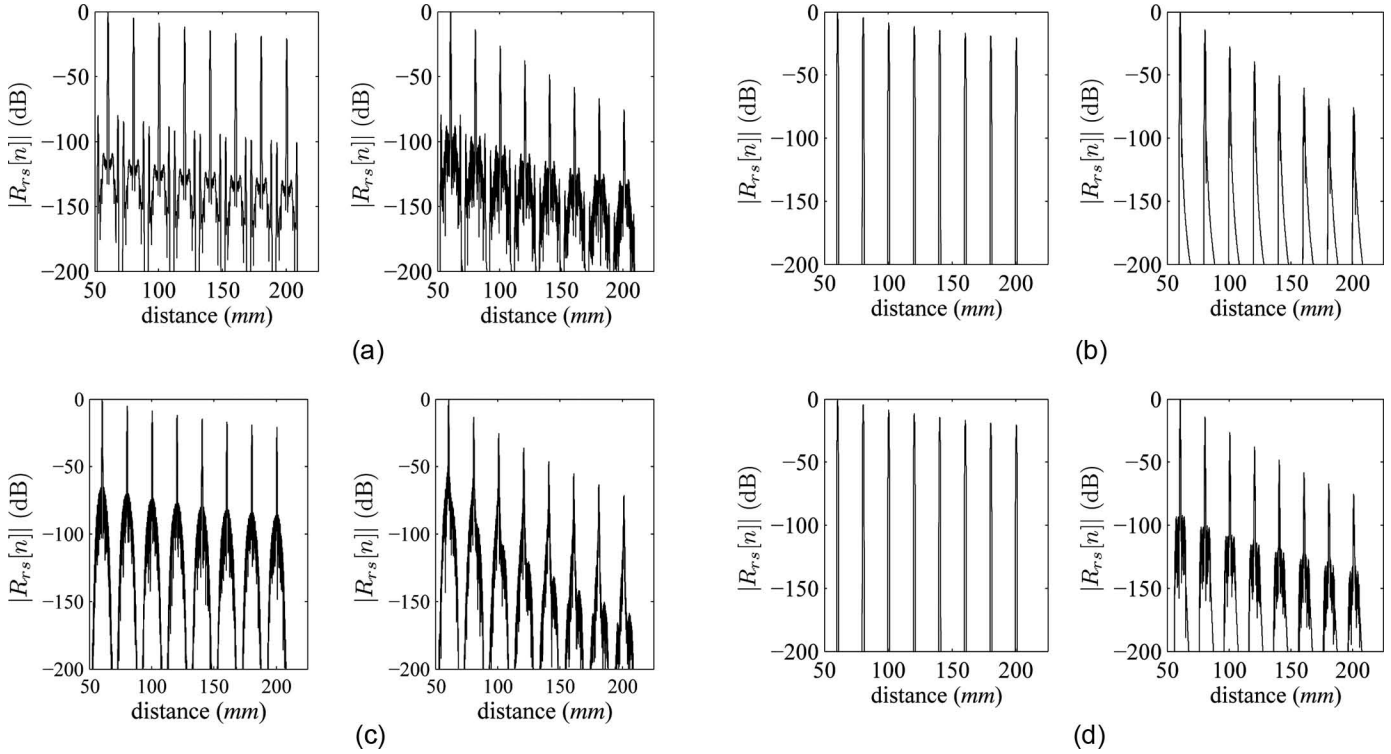

Fig. 17. Compressed central RF-line in (left) frequency-independent and (right) $\beta = 0.7$ dB/(MHz·cm) frequency-dependent attenuating medium for (a) Huffman coding, (b) rectangular-shaped Golay coding, (c) tapered linear-FM coding, and (d) Chebyshev-shaped Golay coding.

not be applied because of the low MSR performance it provides. Fig. 16 shows that the gain in GSNR of TLF with respect to Huffman coding can reach values of around 7 dB for depth ranges between 20 and 30 cm: this fact could make TLF more attractive than Huffman coding in very deep and highly noisy scenarios, especially when the worse performance in MSR is not an issue.

Figs. 17(a)–17(d) show the compressed central RF-line in a frequency-flat attenuating medium and in the same frequency-dependent attenuating medium for Huffman, TLF, R-Golay, and C-Golay coding, respectively. Specifically, eight point-scatterers with equal scattering amplitude have been fixed along the axial direction, spaced 20 mm from each other, at absolute distances ranging from 60 to 200 mm from the transducer, which is modeled as a 32-element phased-array probe. Fixed-focus transmission beamforming at a distance of 100 mm together with dynamic receive beamforming [47] is employed. Figs. 17(a)–17(d) show that Huffman and C-Golay coding outperform all of the other techniques in practical scenarios characterized by frequency-dependent attenuating media.

This can be better appreciated in Fig. 18, which shows the normalized pulse compression output for the four approaches compared in Figs. 17(a)–17(d), in the presence of a single point-scatterer at 150 mm depth. Fig. 18 highlights that both the TLF [Fig. 18(a)] and the R-Golay [Fig. 18(b)] codings are characterized by pronounced side lobes near the main lobe, which is also visibly enlarged. On the contrary, the practical design of the pulse shaping waveform $p[n]$, combined with the almost ideal property (i.e., quasi-Kronecker delta, see Section III) of the codes autocorrelation $R_{cc}[n]$, allows the Huffman [Fig. 18(d)] and the C-Golay [Fig. 18(c)] techniques to obtain the best MSRs. Specifically, at a distance of 150 mm, they still guarantee MSR ≈ 65 and 70 dB, respectively, whereas the

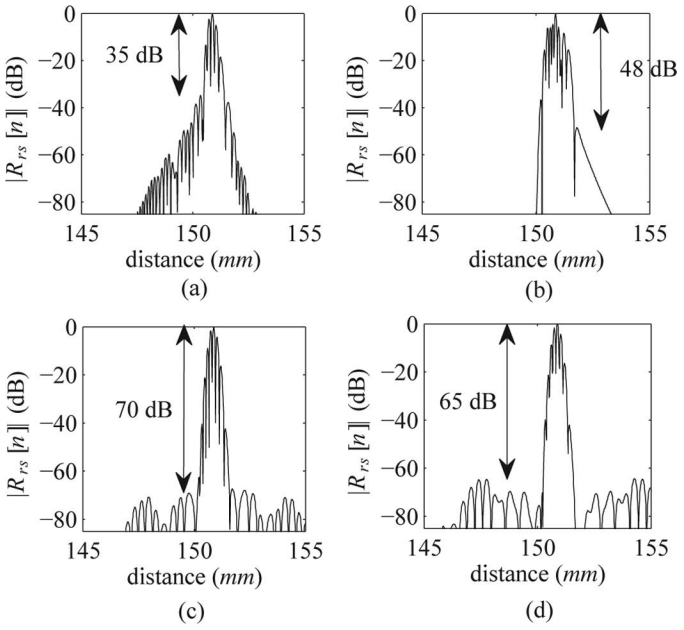

Fig. 18. Normalized compressed central RF-line comparison in $\beta = 0.7$ dB/(MHz·cm) attenuating medium in the presence of a point scatterer at 150 mm distance. (a) Tapered linear FM; (b) rectangular-shaped Golay; (c) Chebyshev-shaped Golay; and (d) Huffman.

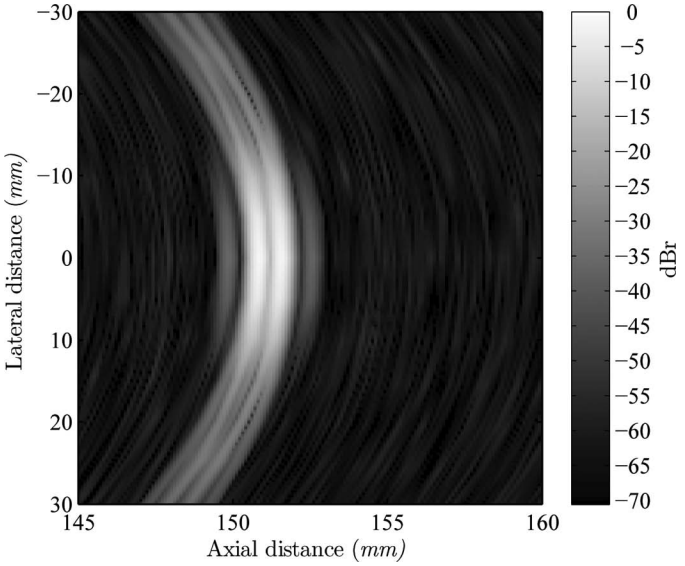

Fig. 19. B-mode image for the proposed Huffman technique.

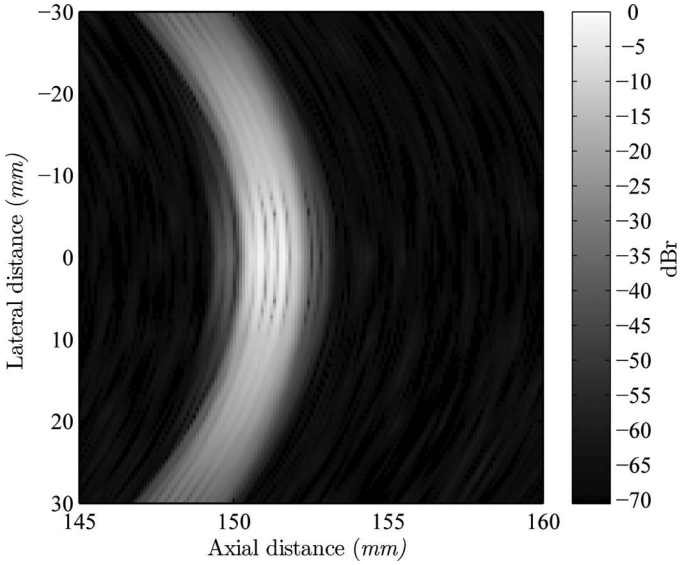

Fig. 21. B-mode image for the rectangular-shaped Golay technique.

TLF and the rectangular-shaped Golay coding schemes give MSR $\approx$ 35 and 48 dB, respectively.

To better highlight the potential advantage provided by Huffman CE, Figs. 19–22 show the zoomed view of B-mode images, obtained with the same Field II parameters used for Fig. 17, with a fixed focus at 100 mm and placing four points scatterers close to each other, at distances 149, 150, 150.7, and 151.7 mm along the axial direction from the transducer. The scattering amplitudes were chosen equal to 0.018, 1, 1, and 0.018 for the increasing distances. This implies that a system with at least 35 dB of dynamic range is needed to correctly show all the scatterers. Note that, without any synthetic dynamic focusing on the transmit side, each point scatterer is perceived as an arc. This effect, which is the same for all of the CE techniques and affects only the lateral resolution, is also useful to better appreciate the differences among different codes in a point-scatterer environment. All of the B-mode images have been produced by a standard log-compression, with a dynamic range of 70 dB, matched to the 128 levels of the gray color bar shown on the right. All of the images are affected by the same white noise, added at the receiver side with a power such that a single element of the array (without beamforming gain) perceives an SNR = −30 dB when there is a single scatterer at 150 mm. Fig. 23 shows the B-mode image obtained without using any coding excitation scheme, and it can be observed that all of the CE techniques are capable of reducing it, proportionally to their GSNR shown in Fig. 16. Moreover, the fixed-focus B-mode images highlight that, although all the CE techniques improve the image quality with respect to the single-pulse transmission, by Huffman and C-Golay coding it is possible to better distinguish the two low reflecting scatterers. Conversely, in the two images obtained

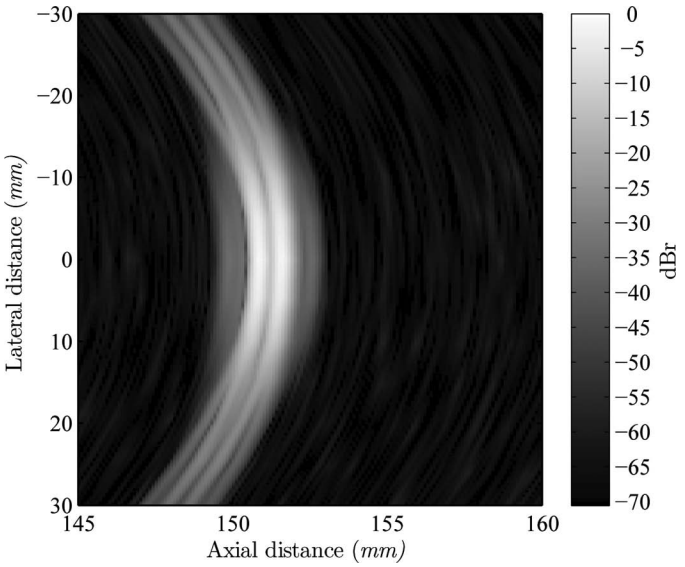

Fig. 20. B-mode image for the tapered linear-FM technique.

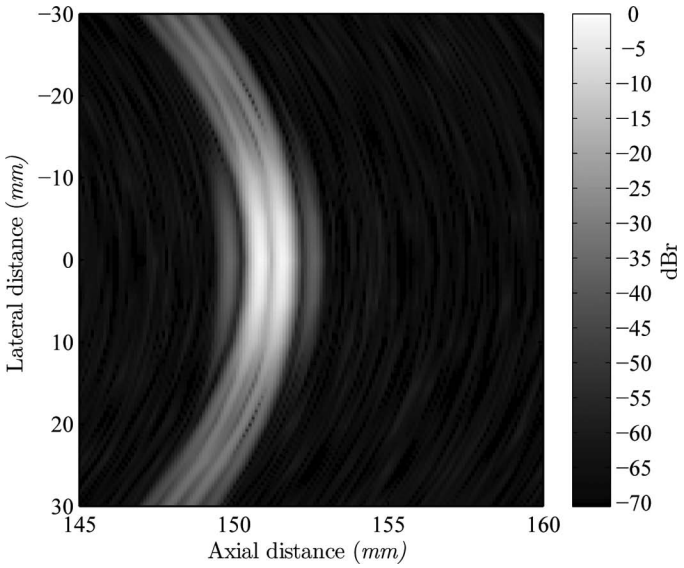

Fig. 22. B-mode image for the Chebyshev-shaped Golay technique.

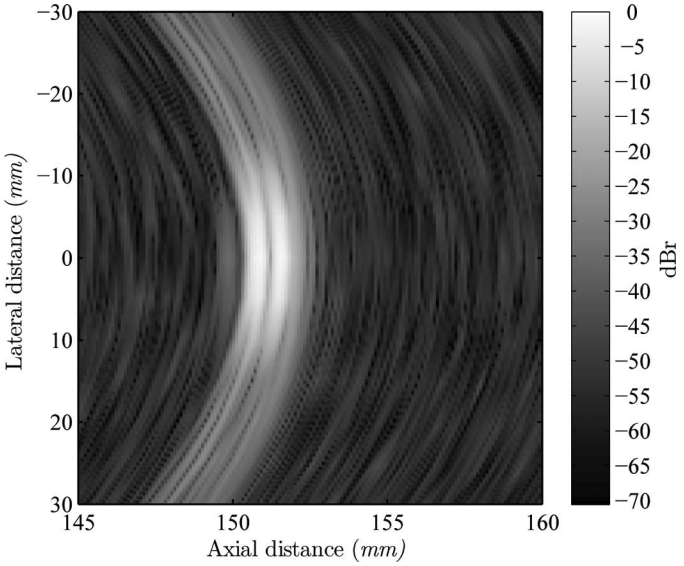

Fig. 23. B-mode image without any coded-excitation technique.

with R-Golay and TLF, the two points with lower scattering amplitudes are not easily distinguishable because they have worse MSRs, as shown in Fig. 18. Moreover, in the R-Golay image of Fig. 21, the two strong scatterers are not distinguishable because of the reduced axial resolution associated with the main lobe enlargement caused by the frequency-dependent attenuation. This effect also partially degrades the TLF coding performance in Fig. 20, although to a much lower extent.

By visual inspection of all of the simulation results shown in this paper, it is possible to conclude that the Huffman technique could also be reasonably preferable to the Chebyshev-shaped Golay approach, because it does not require a double transmission and, consequently, it does not suffer from either a frame-rate reduction or motion artifacts. The Huffman code may also be preferable because it is very robust to frequency-shift induced by moving flow of blood particles in pulse-Doppler applications; this Doppler resistance is due to its ridge-like ambiguity function, shown in Fig. 24, which also highlights that standard complementary Golay codes are characterized by a nonridge-like ambiguity function.

VII. Conclusions and Future Work

This paper has proposed a new approach for coded-excitation in medical ultrasound systems based on the Huffman coding theory [27], and an accurate analytical model to guide a generic linear coded-excitation optimization. The transmitted Huffman sequence is designed by a technique that maximizes the final GSNR and it also provides a good (i.e., a ridge) ambiguity function, which ensures robustness of the system to frequency-shift induced in pulse-Doppler applications. Pulse compression is performed by a matched filtering approach and, notably, it provides superior contrast resolution in almost all conditions; specifically, in the presence of a single scatterer at 150 mm distance in a frequency-dependent attenuation environment, the MSR is roughly 30 and 17 dB better than what it is obtained by the tapered linear-FM proposed in [16] and the (double-transmission) rectangular-shaped Golay coding suggested in [14], respectively. According to the obtained results, the proposed coding may have a considerable impact on CE ultrasound; because this approach has not been widely investigated in the past, there is the potential for further research and optimization. Thus, it can be reasonably expected that, through future investigations, the proposed approach could further outperform currently employed CE schemes. Future work could focus on a procedure to further optimize the choice of the zeros of the Huffman sequence to maximize the sequence effi-

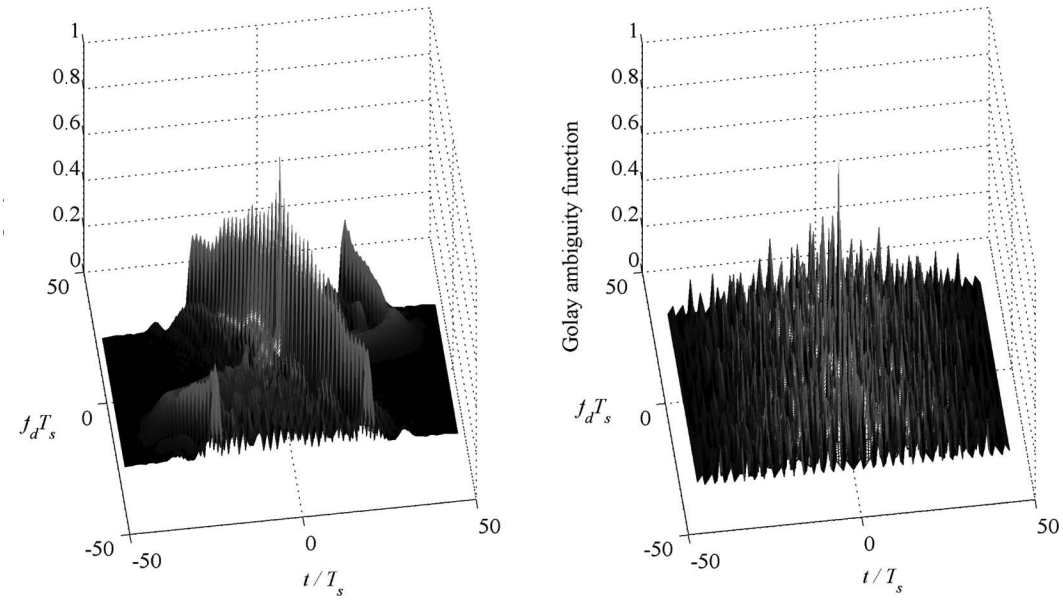

Fig. 24. Comparison of (left) Huffman and (right) Golay code ambiguity functions.

ciency and to fulfill a maximum ISI constraint. Topics for future research include mismatched filtering approaches, dynamic focusing, and time-gain-compensation effects for single-pulse compression after the beamformer, as well as experimental tests on real clinical ultrasound scanners to validate the proposed technique.

Acknowledgments

The authors would like to thank Prof. T. Misaridis for kindly providing the frequency response of the transducer used in [8] and [16] and shown in Fig. 6.

References

[1] B. Angelsen, *Ultrasound Imaging: Waves, Signals, and Signal Processing*. Trondheim, Norway: Emantec AS, 2000.

[2] R. Righetti, S. Srinivasan, and J. Ophir, "Lateral resolution in elastography," *Ultrasound Med. Biol.*, vol. 29, no. 5, pp. 695–704, 2003.

[3] H. Liang, L. Zhou, P. Wells, and M. Halliwell, "Temperature measurement by thermal strain imaging with diagnostic power ultrasound, with potential for thermal index determination," *Ultrasound Med. Biol.*, vol. 35, no. 5, pp. 773–780, 2009.

[4] J. Zachary, J. Sempsrott, L. Frizzell, D. Simpson, and W. O. Brien, "Superthreshold behavior and threshold estimation of ultrasound-induced lung hemorrhage in adult mice and rats," *IEEE Trans. Ultrason. Ferroelectr. Freq. Control*, vol. 48, no. 2, pp. 581–592, 2001.

[5] F. Lizzi and A. Mortimer, "Bioeffects considerations for the safety of diagnostic ultrasound," *J. Ultrasound Med.*, vol. 7, suppl. 9, pp. S1–S38, 1988.

[6] J. Baran and J. Webster, "Design of low-cost portable ultrasound systems: Review," in *Annu. Int. Conf. IEEE Engineering in Medicine and Biology Society*, 2009, pp. 792 –795.

[7] M. Fuller, K. Ranganathan, S. Zhou, T. Blalock, J. Hossack, and W. Walker, "Portable, low-cost medical ultrasound device prototype," in *IEEE Int. Ultrasonics Symp.*, 2004, pp. 106–109.

[8] T. Misaridis and J. Jensen, "Use of modulated excitation signals in medical ultrasound. Part I: Basic concepts and expected benefits," *IEEE Trans. Ultrason. Ferroelectr. Freq. Control*, vol. 52, no. 2, pp. 177–191, 2005.

[9] M. O'Donnell, "Coded excitation system for improving the penetration of real-time phased-array imaging systems," *IEEE Trans. Ultrason. Ferroelectr. Freq. Control*, vol. 39, no. 3, pp. 341–351, 1992.

[10] M. Pollakowski and H. Ermert, "Chirp signal matching and signal power optimization in pulse-echo mode ultrasonic nondestructive testing," *IEEE Trans. Ultrason. Ferroelectr. Freq. Control*, vol. 41, no. 5, pp. 655–659, 1994.

[11] T. Misaridis and J. Jensen, "An effective coded excitation scheme based on a predistorted FM signal and an optimized digital filter," in *IEEE Int. Ultrasonics Symp.*, 1999, vol. 2, pp. 1589–1594.

[12] K. Liu and S. Gao, "Searching binary sequences for coded excitation in medical ultrasound," in *27th Annu. Int. Conf. Engineering in Medicine and Biology Society*, 2005, pp. 1858–1860.

[13] R. Chiao and L. Thomas, III, "Method and apparatus for ultrasonic synthetic transmit aperture imaging using orthogonal complementary codes," Apr. 11, 2000, U.S. Patent 6 048 315.

[14] R. Chiao and L. Thomas, "Synthetic transmit aperture imaging using orthogonal Golay coded excitation," in *IEEE Int. Ultrasonics Symp.*, 2000, vol. 2, pp. 1677–1680.

[15] J. Jensen, O. Holm, L. J. Jensen, H. Bendsen, S. I. Nikolov, B. G. Tomov, P. Munk, M. Hansen, K. Salomonsen, J. Hansen, K. Gormsen, H. M. Pedersen, and K. L. Gammelmark, "Ultrasound research scanner for real-time synthetic aperture data acquisition," *IEEE Trans. Ultrason. Ferroelectr. Freq. Control*, vol. 52, no. 5, pp. 881–891, 2005.

[16] T. Misaridis and J. Jensen, "Use of modulated excitation signals in medical ultrasound. Part II: Design and performance for medical imaging applications," *IEEE Trans. Ultrason. Ferroelectr. Freq. Control*, vol. 52, no. 2, pp. 192–207, 2005.

[17] IEC, "Medical electrical equipment-particular requirements for the safety of ultrasonic medical diagnostic and monitoring equipment," Int. Electrotechnical Commission, Geneva, Switzerland, Tech. Rep. 60601–2-37, 2001.

[18] F. A. Duck, "Medical and non-medical protection standards for ultrasound and infrasound," *Prog. Biophys. Mol. Biol.*, vol. 93, no. 1–3, pp. 176–191, Jan.–Apr. 2007.

[19] C. Cook and M. Bernfeld, *Radar Signals: An Introduction to Theory and Application*. New York, NY: Academic, 1967.

[20] R. Raman and N. Rao, "Pre-enhancement of chirp signal for inverse filtering in medical ultrasound," in *16th Annu. Int. Conf. of the IEEE Engineering in Medicine and Biology Society*, 1994, pp. 676–677.

[21] S. Venkatraman and N. Rao, "Combining pulse compression and adaptive drive signal design to inverse filter the transducer system response and improve resolution in medical ultrasound," *Med. Biol. Eng. Comput.*, vol. 34, no. 4, pp. 318–320, 1996.

[22] M. Oelze, "Bandwidth and resolution enhancement through pulse compression," *IEEE Trans. Ultrason. Ferroelectr. Freq. Control*, vol. 54, no. 4, pp. 768–781, 2007.

[23] J. Cowe, J. Gittins, and D. Evans, "Improving performance of pulse compression in a Doppler ultrasound system using amplitude modulated chirps and Wiener filtering," *Ultrasound Med. Biol.*, vol. 34, no. 2, pp. 326–333, 2008.

[24] M. Benkhelifa, M. Gindre, J.-Y. Le Huerou, and W. Urbach, "Echography using correlation techniques: Choice of coding signal," *IEEE Trans. Ultrason. Ferroelectr. Freq. Control*, vol. 41, no. 5, pp. 579–587, 1994.

[25] M. Ackroyd, "The design of Huffman sequences," *IEEE Trans. Aerosp. Electron. Syst.*, vol. 6, no. 6, pp. 790–796, 1970.

[26] A. Polpetta and P. Banelli, "Huffman sequence design for coded excitation in medical ultrasound," in *IEEE Int. Ultrasonics Symp.*, 2009, pp. 2386 –2389.

[27] M. Ackroyd, "Synthesis of efficient Huffman sequences," *IEEE Trans. Aerosp. Electron. Syst.*, vol. 8, no. 1, pp. 2–8, 1972.

[28] J. A. Jensen, "Field: A program for simulating ultrasound systems," *Med. Biol. Eng. Comput.*, vol. 34, suppl. 1, pt. 1, pp. 351–353, 1996.

[29] J. Jensen, D. Gandhi, and W. D. O'Brien Jr., "Ultrasound fields in an attenuating medium," in *IEEE Int. Ultrasonics Symp.*, 1993, vol. 2, pp. 943–946.

[30] K. Gurumurthy and R. Arthur, "A dispersive model for the propagation of ultrasound in soft tissue," *Ultrason. Imaging*, vol. 4, no. 4, pp. 355–377, 1982.

[31] P. Narayana, J. Ophir, and N. Maklad, "The attenuation of ultrasound in biological fluids," *J. Acoust. Soc. Am.*, vol. 76, no. 1, pp. 1–4, 1984.

[32] J. Jensen, *Estimation of Blood Velocities Using Ultrasound: A Signal Processing Approach*. New York, NY: Cambridge University Press, 1996.

[33] T. Misaridis, M. Pedersen, and J. Jensen, "Clinical use and evaluation of coded excitation in B-mode images," in *IEEE Int. Ultrasonics Symp.*, 2000, vol. 2, pp. 1689–1693.

[34] J. Ophir and P. Jaeger, "Spectral shifts of ultrasonic propagation through media with nonlinear dispersive attenuation," *Ultrason. Imaging*, vol. 4, no. 3, pp. 282–289, 1982.

[35] R. Chiao and X. Hao, "Coded excitation for diagnostic ultrasound: A system developer's perspective," *IEEE Trans. Ultrason. Ferroelectr. Freq. Control*, vol. 52, no. 2, pp. 160–170, 2005.

[36] R. Bjerngaard and J. Jensen, "Should compression of coded waveforms be done before or after focusing?" *Proc. SPIE*, vol. 4687, 2002, pp. 47–58.

[37] T. Misaridis, K. Gammelmark, C. H. Jørgensen, N. Lindberg, A. H. Thomsen, M. H. Pedersen, and J. A. Jensen, "Potential of coded excitation in medical ultrasound imaging," *Ultrasonics*, vol. 38, no. 1–8, pp. 183–189, 2000.

[38] J. Adams, "A new optimal window [signal processing]," *IEEE Trans. Signal Process.*, vol. 39, no. 8, pp. 1753–1769, 1991.

[39] D. Huffman, "The generation of impulse-equivalent pulse trains," *IRE Trans. Inf. Theory*, vol. 8, no. 5, pp. 10–16, 1962.

[40] P. Fan and M. Darnell, *Sequence Design for Communications Applications*. London, UK: Research Studies Press Ltd., Wiley, 1996.

[41] M. Schroeder, "Synthesis of low-peak-factor signals and binary sequences with low autocorrelation," *IEEE Trans. Inf. Theory*, vol. 16, no. 1, pp. 85–89, 1970.

[42] M. Ackroyd, "Computing the coefficients of high-order polynomials," *Electron. Lett.*, vol. 6, no. 22, pp. 715–717, 1970.

[43] F. Harris, "On the use of windows for harmonic analysis with the discrete Fourier transform," *Proc. IEEE*, vol. 66, no. 1, pp. 51–83, 1978.
[44] R. Jırık, T. Taxt, and J. Jan, "Ultrasound attenuation imaging," *J. Electr. Eng.*, vol. 55, no. 7–8, pp. 180–187, 2004.
[45] J. Liu and M. Insana, "Coded pulse excitation for ultrasonic strain imaging," *IEEE Trans. Ultrason. Ferroelectr. Freq. Control*, vol. 52, no. 2, pp. 231–240, 2005.
[46] J. Jedwab and M. Parker, "A construction of binary Golay sequence pairs from odd-length Barker sequences," *J. Comb. Des.*, vol. 17, no. 5, pp. 478–491, 2009.
[47] B. Steinberg, "Digital beamforming in ultrasound," *IEEE Trans. Ultrason. Ferroelectr. Freq. Control*, vol. 39, no. 6, pp. 716–721, 1992.

Alessandro Polpetta received the Laurea degree in electronics engineering and the Ph.D. degree in telecommunications from the University of Perugia, Italy, in 2006 and 2009, respectively. His technical and research interests mainly focus on signal processing and hardware/firmware design for biomedical applications. He is a co-founder (2010) and R&D technical co-director of ICT4Life (http://www.ict4life.it), a spin-off company of the University of Perugia.

Paolo Banelli received the Laurea degree in electronics engineering and the Ph.D. degree in telecommunications from the University of Perugia, Italy, in 1993 and 1998, respectively. In 2005, he was appointed Associate Professor in the Department of Electronic and Information Engineering (DIEI), University of Perugia, where he has been an Assistant Professor since 1998. In 2001, as a visiting researcher, he joined the SpinComm group, led by Prof. G. B. Giannakis, at the Electrical and Computer Engineering Department, University of Minnesota, Minneapolis. His research interests have mainly focused on signal processing for wireless communications, with emphasis on multicarrier transmissions, and more recently, on signal processing for biomedical applications, with emphasis on electrocardiography and medical ultrasound. He has served as a reviewer for several technical journals and as a technical program committee member for leading international conferences on signal processing and telecommunications. In 2009, he was a General Co-Chair of the IEEE International Symposium on Signal Processing Advances for Wireless Communications. In December 2010, he was elected as a member of the SP-COM Technical Committee of the IEEE Signal Processing Society, where he has served since January 2011. He is a co-founder (2010) and scientific co-director of ICT4Life (http://www.ict4life.it), a spin-off company of the University of Perugia.